Mohamed Khider University of Biskra
Faculty of exact sciences and natural and life sciences
Material sciences department

MASTER DISSERTATION

Material sciences
Physics
Energetic Physics and Renewable Energies

Réf. :

Presented by:
DJEFFAL ANOUAR

Le: 26/06/2022

Study of the substitution possibility of Pb by Sn in perovskite solar cell

---

Jury:

LAZNEK Samira	MCB	University of Biskra	President
MEFTAH Afak	Prof	University of Biskra	Supervisor
LAIADI Widad	MCA	University of Biskra	Examiner

Academic Year: 2022

Table of contents

Chapter I : Perovskite materials for solar cells

Chapter II : Design of perovskite solar cell devices

Chapter III : Study of MAPbSn(Cl/I) perovskite solar cell by Silvaco-Atlas

Dedication

I dedicate this work to the best parents ***Djeffal Amara*** *, and* ***Djeffal Zakia***

And my brothers : Abdelhamid, Adel, Fayssal, Issam, Ramzi

And my sisters : Ilham, Leila

Also all my family.

Acknowledgments

First, I would like to thank my advisor, Pr, ***MEFTAH AFAK.*** *Thanks alone is not enough for the amount of help she helped me and the efforts she made to complete this work. Thank you for everything and for your kind treatment.*

Also, I would like to thank all the professors in the field of material sciences.

Also, I would like thank my friends

(Tarek,Moundji,Okba,Mouadh,Madani,Zakaria,Abdelrahman,Mohamed,Aymen, Atef, Yassine…)

*Finally, I would like to thank the members of the jury, Dr.****Laznek Samira*** *and Dr.****laiadi Widad*** *who have kindly accepted to read and examine this work.*

Abstract

The development and commercialization of perovskite solar cells (PSCs) is delayed by the toxicity of lead present in the perovskite, which is the solar light absorber material. To counter this problem, lead (Pb) can be partially replaced by diverse elements and among them we have chosen to study the tin (Sn). The study is based on numerical simulation by Silvaco-Atlas, which is a powerful software for 2D, and 3D electronic device's modelling. The simulated results are also compared with available measurement to certify the study. The studied PSC at the fist is FTO/TiO_2/MAPbI/ spiro-OMeTAD (n-i-p) that gave electrical outputs similar to experimental range; $J_{sc} = 27.91\frac{mA}{cm^2}, V_{oc} = 0.88\,V, FF = 0.72\,, PCE = 17.71\%$.

After that and since the organic HTM (spiro-OMeTAD), according to many works, suffered from instability, we have replaced it by the inorganic HTM CuScN and as results a slight further improvement was occurred in $J_{sc} = 28.15\frac{mA}{cm^2}$. Next we have concentrated on the main goal of the work with is replacing partially Pb by Sn by considering the $MAPbCl_3$ perovskite which has band gap of 2.92 eV. With 80% of Sn and 20% of Pb the band gap is reduced to 2.19 eV and the solar cell gave good electrical outputs similar to experimental data; $J_{sc} = 18.82\frac{mA}{cm^2}, V_{oc} = 1.26\,V, FF = 0.749\,, PCE = 17.76\%$.

The band gap reduction that occurs with the partial replacement of Pb with Sn is used in the design of a Tandem solar cell where the perovskite material of the top cell is $MAPb_{0.2}Sn_{0.8}Cl_3$ (2.19 eV) while that of the bottom one is $MAPb_{0.5}Sn_{0.5}I_3$ (1.18 eV). By considering the ideal performance of the cell a very interesting outputs was obtained: $J_{sc} = 18.82\frac{mA}{cm^2}, V_{oc} = 1.75\,V, FF = 0.804\,, PCE = 26.48\%$.

Key words : perovskite, solar cells, Pb_{1-x}-Sn_x, Silvaco-Atlas.

List of figures

List of tables

List of abbreviations

PSCs	Perovskite solar cells.
FTO	Tin oxide doped with fluorine.
TiO_2	Titanium dioxide.
DSSC	Dye-sensitized solar cell.
HTM	Hole transport material.
ETM	Electron transport material .
SILVACO	Silicon valley corporation.
TCAD	Technology computer aided design.
E_g	Gap energy (eV).
$q\chi_s$	Affinity of the semiconductor (eV).
N_c	Effective density of conduction band (cm^{-3}).
N_v	Effective density of valence band (cm^{-3}).
μ_n	Elctron mobility ($cm^2V^{-1}s^{-1}$).
μ_p	Hole mobility ($cm^2V^{-1}s^{-1}$).
ε_r	Relative dielectric constant.
I_{SC}	Short circuit current (A).
V_{OC}	Open circuit voltage (V).
FF	Fill factor.
PCE	Power conversion efficiency.
HOMO	Highest occupied molecular orbital.
LUMO	Lowest unoccupied molecular orbital.

Introduction

Introduction

During the past decade, hybrid halide perovskites (HPs) have attracted excessive consideration from the scientific community worldwide for a large range of optoelectronic applications [1] such as lasers [2], light emitting diodes [3], photodetectors [4], scintillation [5], and photovoltaic solar cells [6]. For the latter, they have developed as very promising alternatives or complements to silicon solar cells by integrating them in monojunction or multijunction devices [1]. The first report on the use of hybrid halide perovskite was published in 2009 by Miyasaka et al. [7] and related the integration of dispersed perovskite nanocrystals into a mesoporous TiO_2 layer to produce an unstable dye-sensitized solar cell (DSSC) that attained a maximum power conversion efficiency (PCE) of 3.8% [1]. After the replacement of the liquid electrolyte by a solid-state hole transporting material (HTM) in 2012 [8], hybrid halide perovskites have been widely studied due to their semiconductor properties such as high absorption coefficient and large absorption wavelength range [9], high charge carrier mobility [10], extended free carrier diffusion length [11], and tunable bandgap [12]. Appearance of solid-state perovskite-based solar cells using solid perovskite films and called perovskite solar cells (PSCs) started with different papers reporting PSCs using $CsSnI_3$ and $MAPbI_3$ perovskite absorber and achieving PCE above 10% [8]. In few years, PCE of PSCs have quickly increased to reach a certified PCE of 25.5% in 2020 [13], comparable with those of commercially available silicon solar cells. To get such high efficiency, different lead (Pb)-based absorber thin films have been developed such as $CsPbI_3$, $MAPbI_3$, $FAPbI_3$ (MA¼ methylammonium FA¼ formamidinium) or compounds with mixed-cations and/or mixed-halides [14].

However, Pb-based perovskites suffer from two main problems: a rather poor stability and high toxicity [1]. Concerning the stability, different approaches have been developed to overcome this problematic: device engineering, use of 2D perovskites (2D or quasi-2D perovskites), of barrier layers, perovskite stabilization by device encapsulation [1,15]. In contrast, the toxicity of lead seriously burdens the development, industrialization, and large-scale production for PSCs [1] . This toxicity presents risks not only for the human and animals health [16] but also, to the environment. Indeed, lead can spread easily in nature, in plants, in animals and be concentrated in the food chain [17]. Consequently, it becomes compulsory to totally eliminate or partially replace lead from PSCs with other less-toxic elements. However, substituting lead by another element remains uneasy and a major concern [1].

The first study of Sn-based hybrid halide perovskite was carried out in 1974 by Fischer et al. who made and characterized $CsSnX_3$ with X being Cl, Br, and I [18]. Later, different groups pursued the investigation of those materials to determine their nature, even with dimension reduction [19] until it was verified that they are indeed semiconductors [1].

The aim of this master dissertation is the study of the possibility of replacing partially Pb by Sn in two different perovskite materials; $MAPbCl_3$ and $MAPbI_3$. The solar cell structure is the standard n-i-p. The top contact is FTO, the n layer is TiO_2 (named ETL) and the bottom contact is Ag (silver). However for the p layer two materials are suggested: organic Spiro-OMeTAD and inorganic CuScN. The study is carried out by numerical simulation tool, Silvaco-Atlas, and compared to experimental data from other works. The dissertation is divided into three chapters, introduction and conclusion. The two first chapters are on the state of the art of the perovskite material and the solar cells based on of the different perovskites. In addition, the toxicity issue of the Pb was included while the third chapter elucidate the use of Silvaco-atlas and the simulation results concerning the partial replacing of Pb by Sn. First in single n-i-p then in tandem n-i-p/n-i-p solar cells.

Chapter I

Perovskite materials for solar cells

Chapter I: Perovskite materials for solar cells

I.1 History of perovskite materials

Since the discovery of the photovoltaic effect by *Becquerel* in 1839 [20] many types of photovoltaic materials have been tested. Some of these materials are still used today and are found in solar cell efficiency charts [13,21,22]. However, only a few high-performance materials have been commercialized, i.e., gallium arsenide (GaAs), silicon (Si), copper indium gallium sulfurselenide (CIGS, CIGSSe), and cadmium telluride (CdTe). The current champion single-cell efficiencies of GaAs, Si, CIGS, CdTe, and a-Si are 29.1% at 0.998 cm^2 , 26.7% at 79.0 cm^2, 23.4% at 1.043 cm^2, 22.1% at 0.4798 cm^2, and 14.0% at 1.045 cm^2, respectively. The corresponding module efficiencies are 25.1% at 866.45 cm^2, 24.4% at 13 177 cm^2, 19.2% at 841 cm^2 , 19.0% at 23 573 cm^2 , and 12.3% at 14 322 cm^2 , respectively [13,21,22].

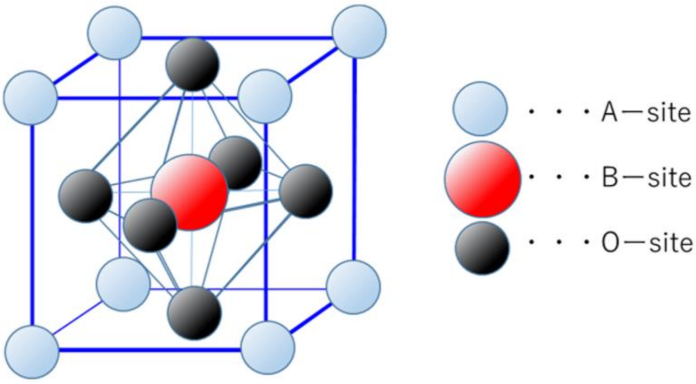

Figure I.1: Perovskite structure (ABO structure) [23].

"Perovskite" is the name of a crystal structure, which was found by a Russian scientist, *Lev Perovski* and the structure was based on cubic structure and was composed of three elements as ABX_3 (**Figure I.1**). He found the oxide perovskite, which has been a famous crystal and ceramic for scientists, and is quite stable against circumstances. The oxide perovskite crystal is composed of "2+" metal cation in the A site, "4+" metal cation in the B site, and "2−"oxygen anion in the O site. The most famous perovskite crystals are $CaTiO_3$ and $BaTiO_3$. Afterwards, Wells found another style of perovskite crystal, composed of "1+" alkaline cation (Cs^+ and K^+), "2+" lead cation (Pb^{2+}), and 1− halogen anion (I^-, Br^-, and Cl^-) in 1893 [24]. In 1978, Weber found the possibility of utilization of methyl ammonium cation ($CH_3NH_3^+$) for the components in lead-halide perovskite crystals [25].

In 1995, *Mitzi et al*. reported the 2-dimensional organo-lead-halide perovskite crystal with a special function of semiconducting in science [26] resulting in a big impact on the scientific society and a big research project in Japan (*CREST*).

Afterwards, a scientist named *Teshima* in the *CREST* project (*Japan*) shifted out to Laboratory of Miyasaka, who worked on dye-sensitized solar cells, and published the first paper in *JACS* about $CH_3NH_3PbX_3$ ($X = I^-$ and Br^-) perovskite solar cells while supervising a former student named *Kojima* at 2009 [7]. Initially, perovskite solar cells did not receive much attention because of their poor stability and efficiency. However, research has increased since *Park* and co-workers reported an efficiency exceeding 9% with stability over 500 h in ambient conditions [27,28]. In the last six years, the efficiency of perovskite solar cells increased from 14.1% to 25.2%, which is the third highest single-junction efficiency reported thus far [13,21,22].

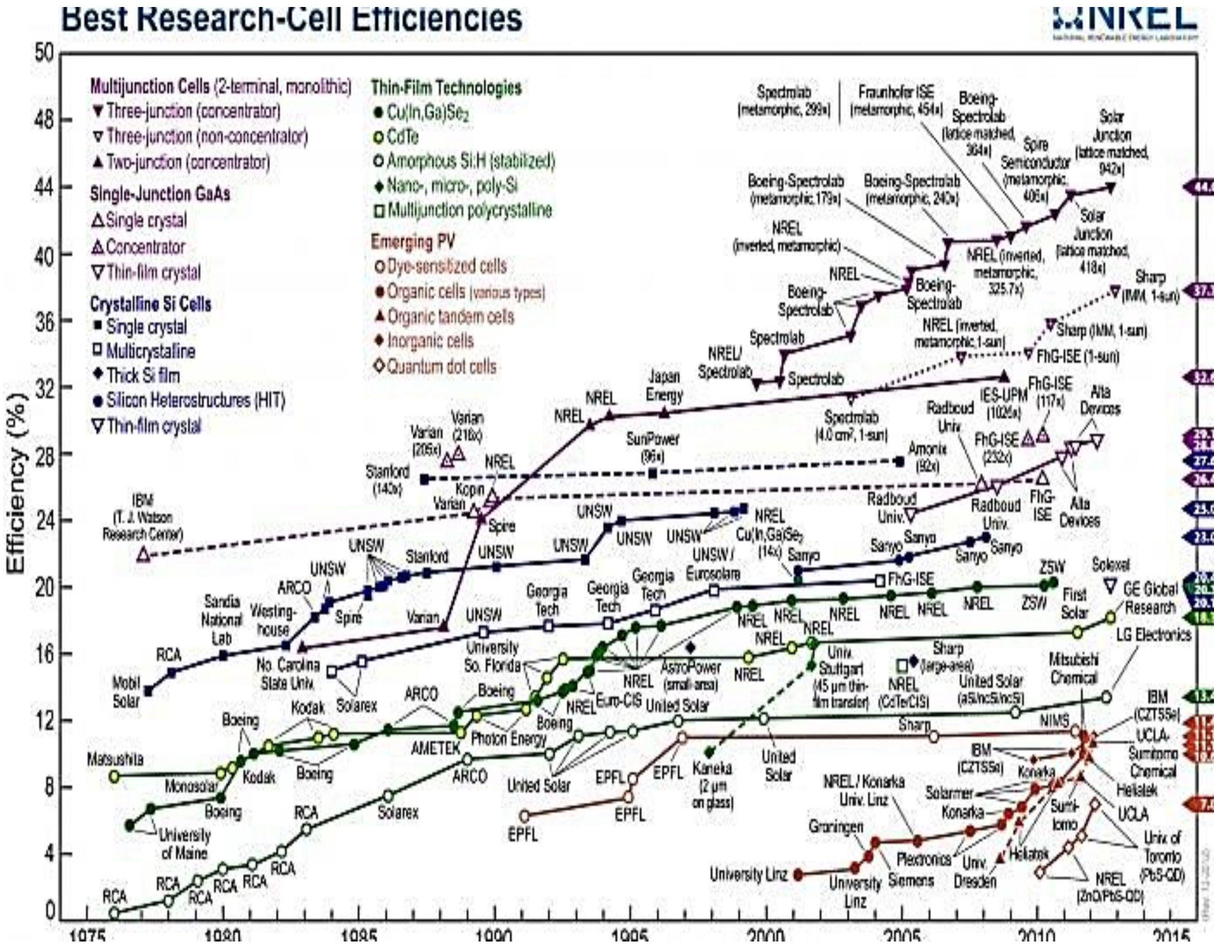

Figure I.2: NREL Best Research-Cell Efficiency Chart [13].

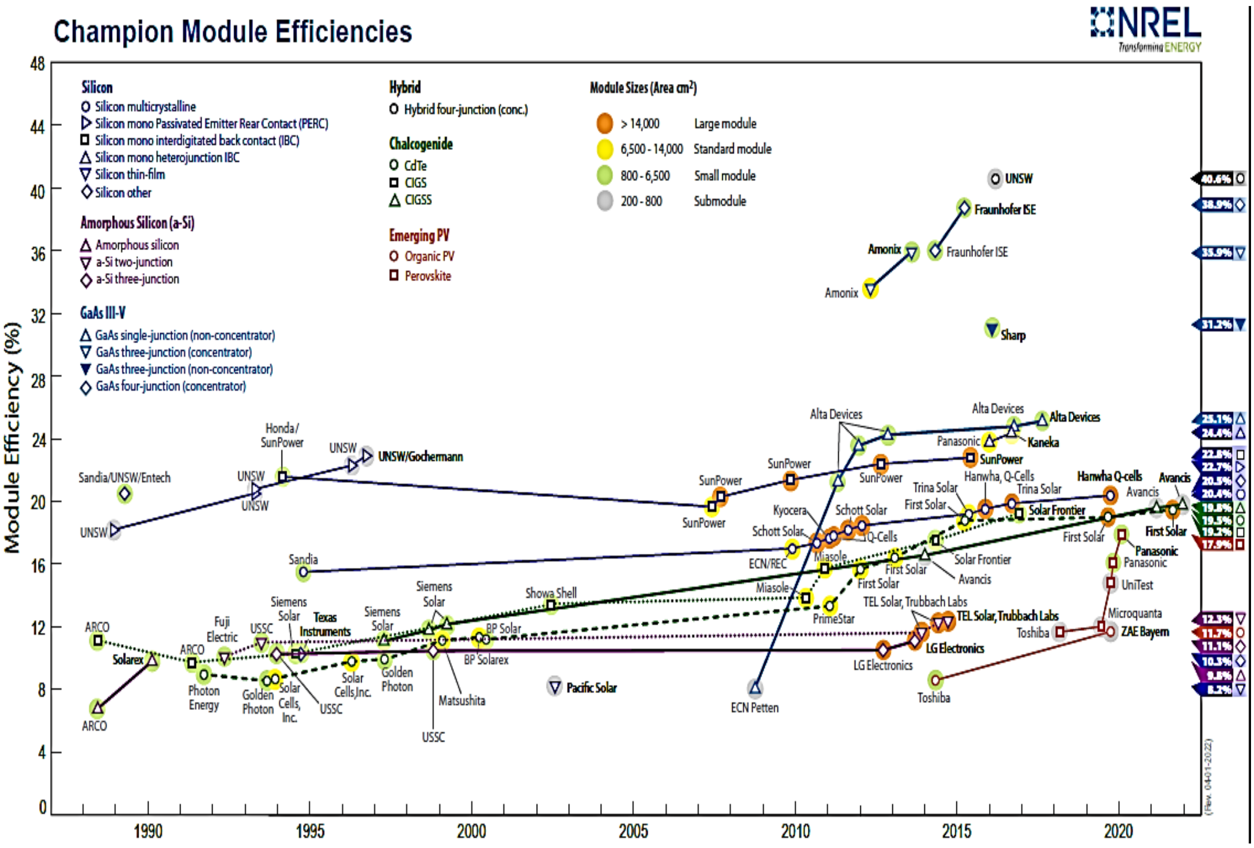

Figure I.3: NERL Champion Photovoltaic Module Efficiency Chart [21].

I.2 Perovskite crystal structure

The perovskite structures used for solar cell devices often have a chemical composition of ABX_3, where A is generally a monovalent cation, B is a divalent cation, and X is a monovalent halogen anion.

A basic structural model of ABX_3 perovskite is shown in **Figure I.4** where the B cation forms BX_6 octahedron. For example let us take the $CH_3NH_3PbI_3$ crystal, A^+ is CH_3NH^{+3}, B^{2+} is Pb^{2+}, and X^- is I^- [29].

From a crystallographic perspective, the ideal perovskite structure is inflexible, as the unit cell has no adjustable atomic position parameters, so that any compositional change must be accommodated by a change in lattice parameter. **Figure I.5** gives the $SrTiO_3$ as a comprehensive example.

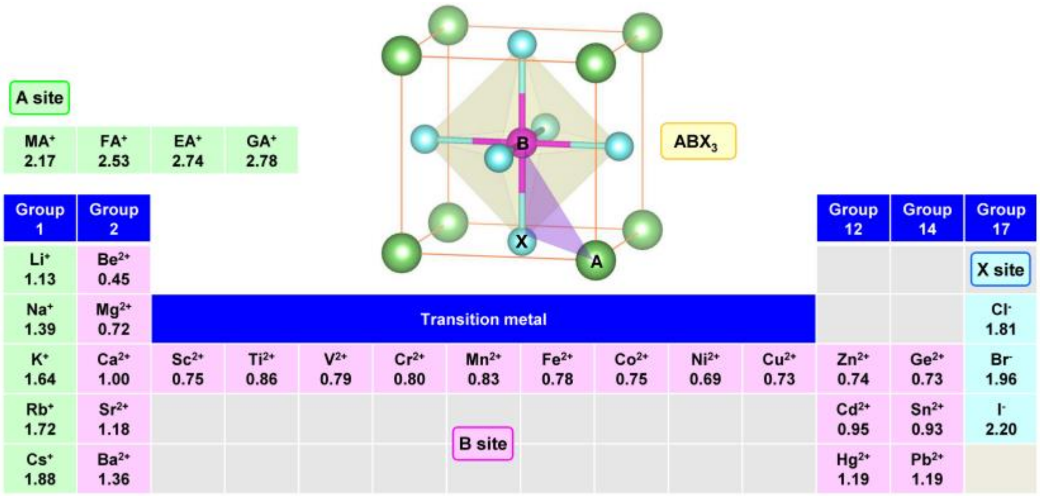

MA$^+$	FA$^+$	EA$^+$	GA$^+$
2.17	2.53	2.74	2.78

Group 1	Group 2										Group 12	Group 14	Group 17
Li$^+$ 1.13	Be^{2+} 0.45												X site
Na$^+$ 1.39	Mg^{2+} 0.72	Transition metal											Cl$^-$ 1.81
K$^+$ 1.64	Ca^{2+} 1.00	Sc^{2+} 0.75	Ti^{2+} 0.86	V^{2+} 0.79	Cr^{2+} 0.80	Mn^{2+} 0.83	Fe^{2+} 0.78	Co^{2+} 0.75	Ni^{2+} 0.69	Cu^{2+} 0.73	Zn^{2+} 0.74	Ge^{2+} 0.73	Br$^-$ 1.96
Rb$^+$ 1.72	Sr^{2+} 1.18					B site					Cd^{2+} 0.95	Sn^{2+} 0.93	I$^-$ 2.20
Cs$^+$ 1.88	Ba^{2+} 1.36										Hg^{2+} 1.19	Pb^{2+} 1.19	

Figure I.4: Structural model of ABX$_3$ perovskite and ionic radii (Å) of elements and molecules [29].

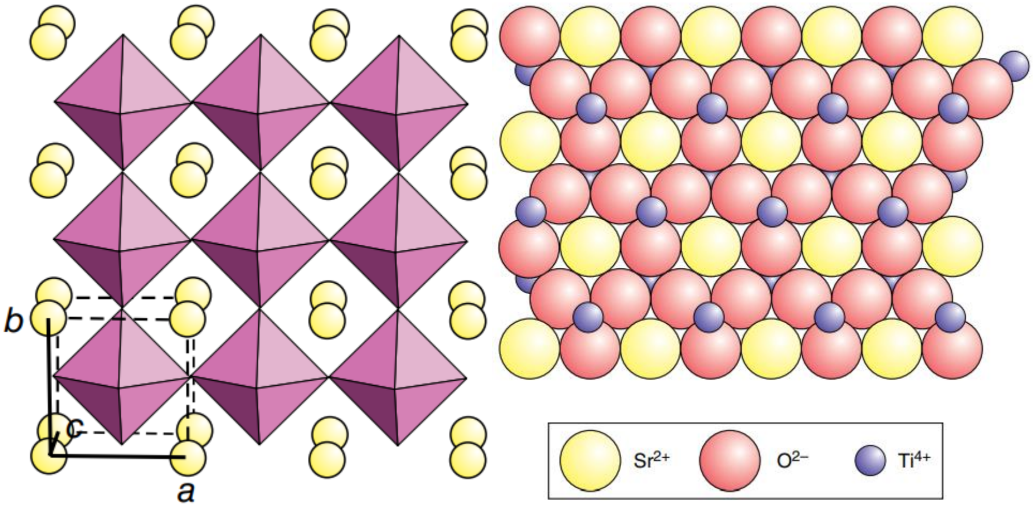

Figure I.5: The cubic SrTiO$_3$ perovskite structure conventional view with 3×3×1 unit cells displayed (ON THE LEFT), Atomic perspective overlay showing A single SrO$_3$ (111) plane in SrTiO3 . The Ti4+ ions, above and below the SrO$_3$ layer, occupy octahedral interstices that are bounded by six O^{2-} ions(ON THE RIGHT) [30].

While for the hybrid Organic–Inorganic Perovskites, the A-sites in the perovskite structure are large enough to accommodate a number of complex ions including ammonium $(NH_4)^+$;

methyl- ammonium $(CH_3NH_3)^+$ frequently written as MA; tetramethylammonium,$[(CH_3)_4N]^+$, frequently written as TMA and formamidinium $(NH_2{=}CHNH_2)^+$, written as FA. The most important of these are the compounds formed with the Group 14 elements Ge, Sn and Pb, together with a halogen Cl, Br and I (**Table I.1**).

The valence state of the organic ion is +1, and this necessitates the B cation to adopt the +2 state. It is unusual to find these large B^{2+} ions in the octahedral B-sites, and they are more frequently associated with A-sites, as in lead titanate, $PbTiO_3$. A large electropositive cation is needed in the A-site to achieve this, which can include the inorganic cation Cs^+ as well as the ions above, and it is convenient to group the Cs halide perovskites with these inorganic–organic phases. The structure of these materials is typically slightly distorted cubic [30].

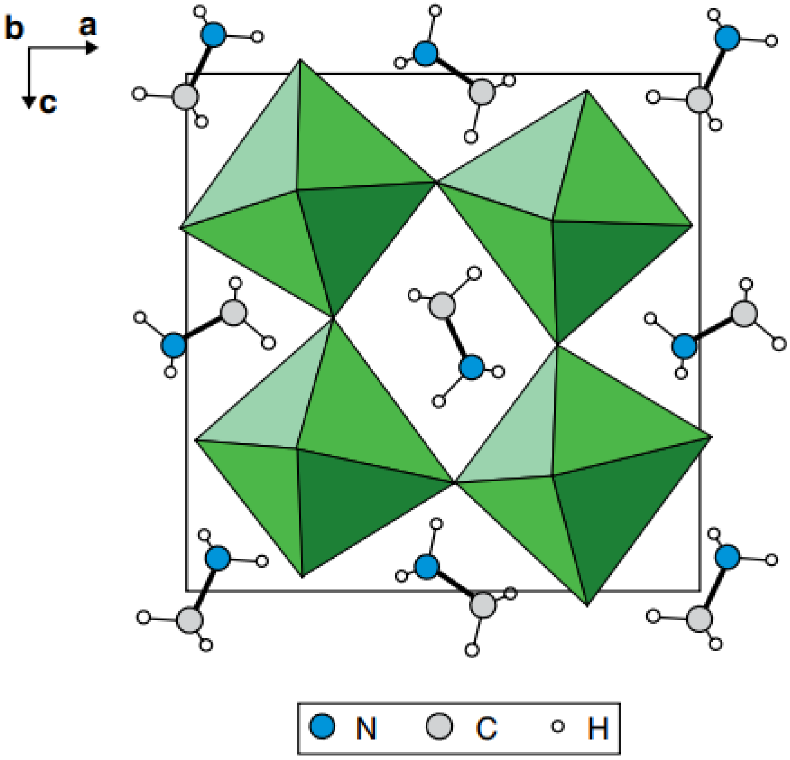

Figure I.6: The structure of $(CH_3NH_3)PbCl_3$ ($MAPbCl_3$). One layer of the structure is shown. Inpreceding and succeeding layers, the organic molecules are rotated by 180° compared to that drawn [30].

Table I.1: Organic–inorganic hybrid and related perovskites [30].

Phase	Space groupe	a (nm)	b (nm)	c (nm)	Angles(°)	Temp (°K)
$CsSnI_3$	O, Pnma (62)	0.86885	1.23775	0.86384		300
$CsSnI_3$	T, P4/mbm (127)	0.87182		0.61908		350
$CsSnI_3$	C, $Pm\bar{3}m$ (221)	0.62057				478
$MAGeCl_3$	M, $P2_1/n$ (14)	1.09973	0.72043	0.82911	α, 90.47	2
$MAGeCl_3$	O, Pnma (62)	1.11567	0.73601	0.82936		250
$MAGeCl_3$	Tr, R3m (160)	0.56784			α, 90.95	370
$MAGeCl_3$	C, $Pm\bar{3}m$ (221)	0.56917				475
$CD_3ND_3GeCl_3$	M, $P2_1/n$ (14)	1.09973	0.72043	0.82911	β, 90.47	2
$CD_3ND_3GeCl_3$	O, Pnma(62)	1.11567	0.73601	0.82936		250
$CD_3ND_3GeCl_3$	Tr, R3m (160)	0.56584			α, 90.95	370
$CD_3ND_3GeCl_3$	C, $Pm\bar{3}m$ (221)	0.56917				475
$MASnCl_3$	Tri, P1 (1)	0.5726	0.8227	0.7910	α, 90.40	297
					β, 93.08	
					γ, 90.15	
$MASnCl_3$	M, Pc (7)	0.5718	0.8326	0.7938	β, 93.03	318
$MASnCl_3$	Tr, R3m (160)	0.5734			α, 91.90	350
$MASnCl_3$	C, $Pm\bar{3}m$ (221)	0.5760				478
$MASnBr_3$	O, $Pmc2_1$ (26)	0.58941	0.83862	0.82406		215
$MASnI_3$	T, P4mm (99)	0.62302		0.6231		293
$MASnI_3$	T, *I*4cm (108)	0.87577		1.2429		200
$MAPbI_3$	T, P4mm (99)	0.63115		0.63161		400
$MAPbI_3$	T, *I*4cm (108)	0.8849		1.2642		293
$MAPbI_3$	O, Pnma(62)	0.88362	1.25804	0.85551		100
$FASnI_3$	O, Amm2 (38)	0.63286	0.89554	0.89463		340
$FASnI_3$	O, *I*mm2 (44)	1.25121	1.25171	1.25099		180
$CH_3ND_3PbCl_3$	O, Pnma(62)	1.11747	1.13552	1.12820		80
$CH_3ND_3PbCl_3$	C, $Pm\bar{3}m$ (221)	0.5669				280
$CH_3ND_3PbBr_3$	O, Pnma(62)	0.79434	1.18499	0.85918		11
$MAPbI_3$	O, Pnma(62)	0.88362	1.25804	0.85551		100
$MAPbI_3$	T, *I*4/mcm (140)	0.8851		1.2444		298
$MAPbI_3$	C, $Pm\bar{3}m$ (221)	0.6274				333
$FAPbI_3$	Tr, P3m1 (156)	0.89817		1.1006	γ, 120	293

This is a simple sum of anion – cation bond lengths. The cubic unit cell edge, a, is equal to twice the B─X bond length:

$$2(B-X)=a \tag{I.1}$$

The width of the cuboctahedral cage site, $\sqrt{2}a$, is equal to twice the A─X bond length:

$$2(A-X)=\sqrt{2}a \tag{I.2}$$

This means that the ideal structure forms when the ratio of the bond lengths is given by:

$$\frac{A-X}{B-X}=\sqrt{2} \quad or \quad \frac{A-X}{(\sqrt{2})(B-X)}=1 \tag{I.3}$$

Goldschmidt first exploited this relationship in 1926 [30]. who suggested that it could be used to predict the likelihood that a pair of ions would form a perovskite structure phase. When this was initially proposed, very few crystal structures had been determined and so ionic radii were used as a substitute for measured bond lengths. For this purpose, it is assumed that for a stable structure to form the cations, just touch the surrounding anions (Goldschmidt's rule), then [30]:

$$\frac{(r_A+r_x)}{(r_B+r_x)}=\sqrt{2} \quad or \quad t=\frac{(r_A+r_x)}{(\sqrt{2})(r_B+r_x)}=1 \;\; (ideal\ structure) \tag{I.4}$$

Wheret is called the tolerance factor, r_A is the radius of the cage site cation, r_B is the radius of the octahedrally coordinated cation and r_X is the radius of the anion. Goldschmidt's proposal was that a perovskite structure phase would form if the value of the tolerance factor, t, was close to 1.0.

Note that it is necessary to use ionic radii appropriate to the coordination geometry of the ions. Thus,r_A should be appropriate to 12 coordination, r_B to octahedral coordination and r_X to linear coordination. Furthermore, it is best to use radii scales that mirror the X anion present, as radii appropriate to oxides, although a reasonable approximation for fluorides, are poor when applied to chlorides and sulphides. Because many perovskite structures have been described, it is now usual to use the measured bond lengths in the crystal rather than ionic radii to give an observed tolerance factor t_{obs} [30]:

$$t_{obs}=\frac{A-X}{(\sqrt{2})(B-X)} \tag{I.5}$$

Where (A─X) is the average of the measured bond lengths between the A cation and the surrounding 12 anions and (B─X) is the average of the measured bond lengths between the B cation and the surrounding six anions. It is found that for specific groups of perovskites (e.g. $ATiO_3$ titanates, $AAlO_3$ aluminates), there is a linear relationship between t obs and t which varies slightly from one family to another [30].

However, it is not enough to deduce the probable crystallographic structure of perovskite materials by only considering tolerance factors. Therefore, the octahedral factor "μ" is used as an additional indicator to predict the formation of perovskite structure, should lie between ***$0.44 < \mu < 0.90$*** for stable perovskite structures and is given by the equation [31–33]:

$$\mu = \frac{r_A}{r_x} \qquad \text{(I.6)}$$

Whereas the tolerance factor (t) and the octahedral factor (μ) are two important factors to quantify the structure and stability of perovskite [34].

I.3 Electronic structure of perovskites

In the hybrid perovskite structure of $CH_3NH_2PbI_3$, the metal has an occupied s orbital (lone pair) whose electrons interact strongly with the in-plane anion p states forming an anti-bonding state as the top of the VB with mostly s-orbital character. The CB minimum is constituted from anti-bonding Pb(6p)-I(5p) states with a p orbital character [35].

The substitution of the monovalent Acation does not directly affect the electronic band structure in halide perovskites [36], Both VB and CB are formed by anti-bonding orbitals. The anti-bonding structure contributes to suppression of charge recombination leading to superior photovoltaic property such as high voltage generation. **Figure I.8** shows a high symmetry of band structure, which enables direct p-p electron transition from VB to CB [37].

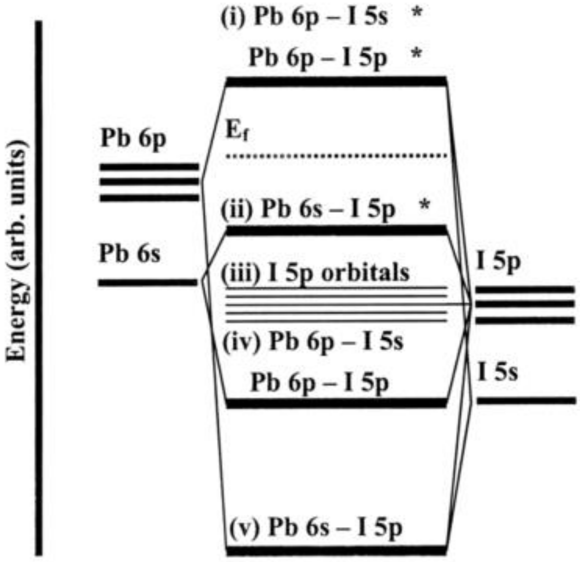

Figure I.7: Bonding diagram of a $[PbI_6]^{-4}$ cluster, representing the perovskite $MAPbI_3$ [38].

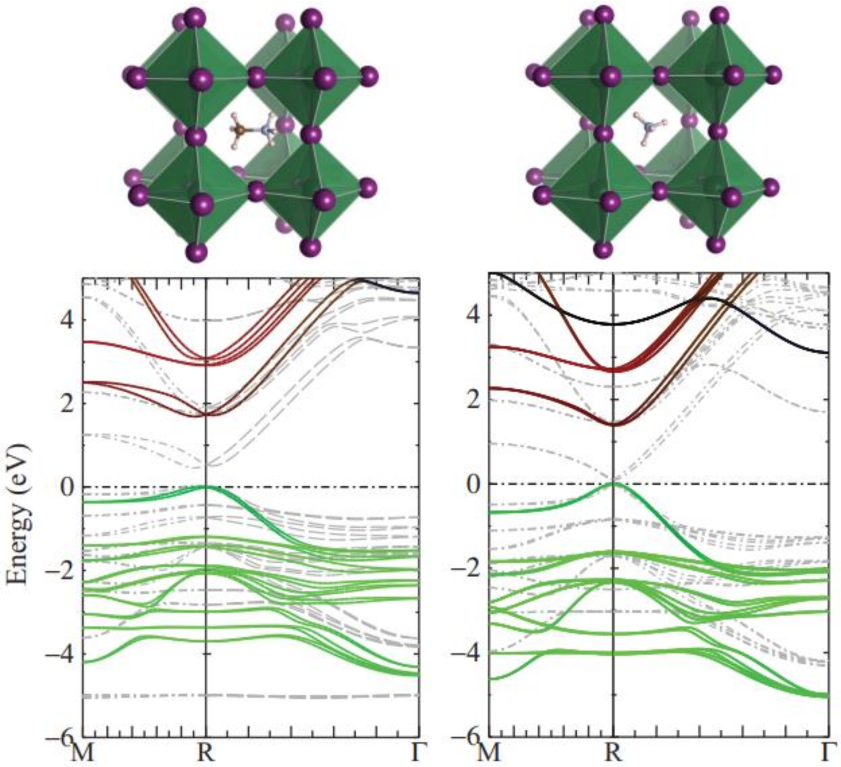

Figure I.8: (Color online) QSGW band structure for $CH_3NH_3PbI_3$ (ON THE LEFT) and NH_4PbI_3 (ON THE RIGHT). Zero denotes valence band maximum. Bands are colored according to their orbital character: green depicts I 5p, red depicts Pb 6p, and blue depicts Pb 6s [39].

I.4 Deposition methods of perovskite films

To deposit perovskite films through solution processing, organic halides and lead halides are first dissolved in organic solvents such as N,N-dimethylformamide (DMF), dimethyl sulfoxide (DMSO) and γ-butyrolactone (GBL). These perovskite precursor solutions are used in both spin coating and scalable deposition methods. Spin coating is the most common method for perovskite thin-film deposition. However, it is generally limited to a scale of 90% of the precursor ink is wasted in the process. Modules can be fabricated by spin coating on a substrate area of up to about 10cm×10cm but with a considerably lower PCE than their smaller-area counterparts [40].

In spin coating, thinning and smoothing of the wet-solution films rely on the continuous centrifugal force from spinning, which is difficult to replicate in scalable deposition processes. Thus, the solution chemistry and processing conditions developed for spin coating cannot be easily applied in other scalable deposition methods. Furthering our understanding of the factors that affect thin-film formation and increasing our control of thin-film formation in different deposition processes are crucial for scaling up PSCs [41].

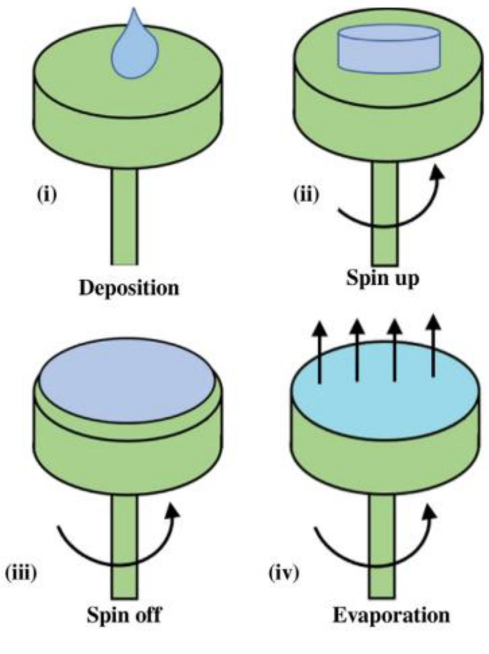

Figure I.9: Spin coating process [42].

I.4.1 Scalable deposition techniques

The following table resembles a brief description of some common used scalable deposition techniques for perovskite thin layers production:

Table I.2: Common perovskite scalable deposition techniques

Technique	**Principal**	**Controlling factors**	**Reference**
Blade coating	Spreading the precursor solution with a blade to form a thin film on the substrate.	-Precursor solution concentration. -The gap between the blade and substrate. -Blade movement speed.	[43,44]
Slot-die coating	Applying the precursor over the substrate with a thin slit.	-Same as blade coating. -Better yield and reproducibility with developed ink	[41,45]
Spray coating	Using a nozzle to disperse tiny droplets on substrate.	-Spraying method (*pneumatic, ultrasonic and electro-spraying*). -Solventratio and precursor temperature. -The voltage and electrical Field tuning (*Electro-spray*ing).	[46–51]
Inkjet printing	Using a nozzle to disperse precursor ink on substrate.	-Adjustable droplet size and trajectory. -Distance between the nozzles and Substrate	[52]
Screen printing	Transferring to the substrate via patterned Mesh.	-Mesh size -Thickness of emulsion layer.	[52]

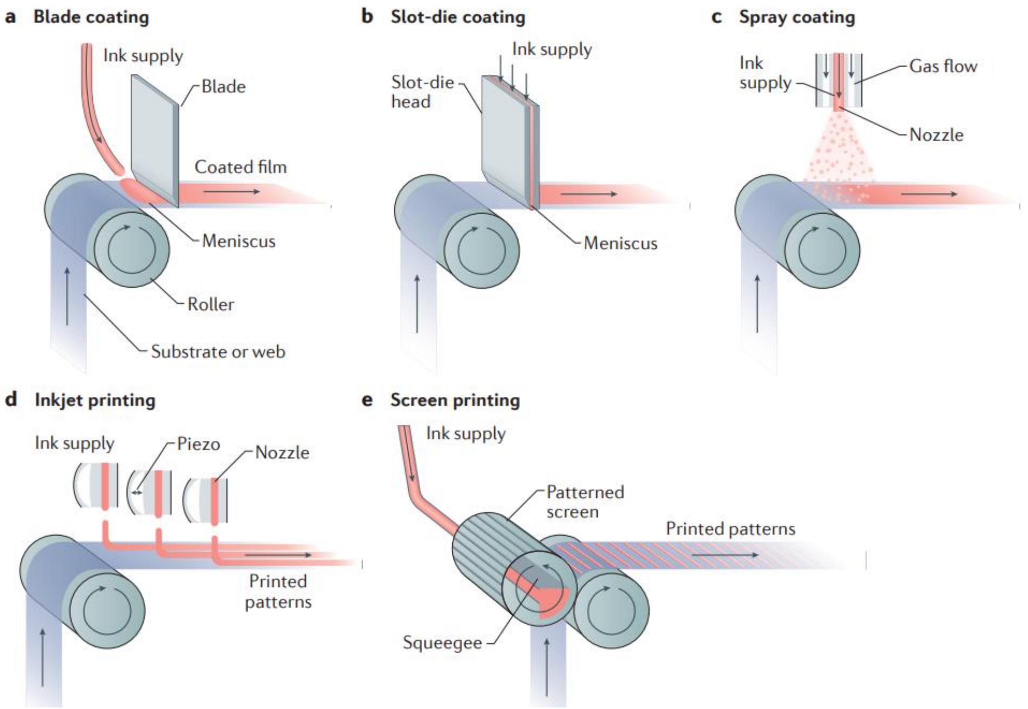

Figure I.10: Common scalable solution deposition methods for the roll-to-roll fabrication of perovskite solar cells [41].

I.4.2 Single step, Two-steps deposition

The two-step deposition method was developed for deposition of perovskite films in a low temperature, as a second way to improve deposition in one-step that results in poor surface coverage showing non-uniformity. The two-step deposition method does not required a complete precursor preparation but separates the coating of PbI_2 and MAI, a thin film is first deposited using metal halide PbI_2 precursor using spin coating process mostly and then the film coated substrate is dipped into the second precursor solution MAI the final perovskite films would be formed after proper baking. Although steps become more complicated [53–55].

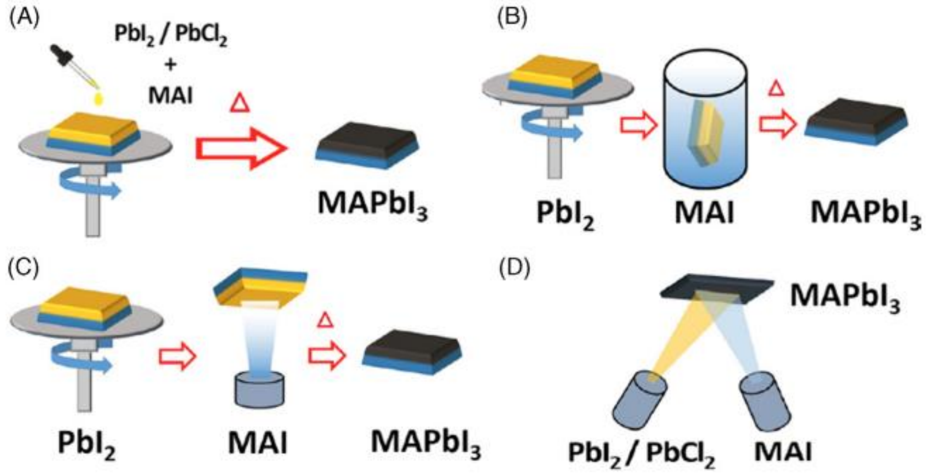

Figure I.11: Deposition methods for perovskite thin films, including (A) single-step solution deposition, (B) two-step solution deposition, (C) two-step hybrid deposition, and (D) thermal vapour deposition [56].

I.4.3 Thermal vapour deposition

The thermal evaporation method utilizes a dual source for MX_2 and MAI or FAI (Formamidinium iodide) with different heating elements to form perovskite films [57].this method provides high-quality perovskite thin film with a uniform thickness and of pin-hole-free composition. The first planar heterojunction $MAPbI_{3-x}Cl_x$ solar cell was fabricated in 2013 using thermal vapour deposition technique with efficiency of >15% [57].

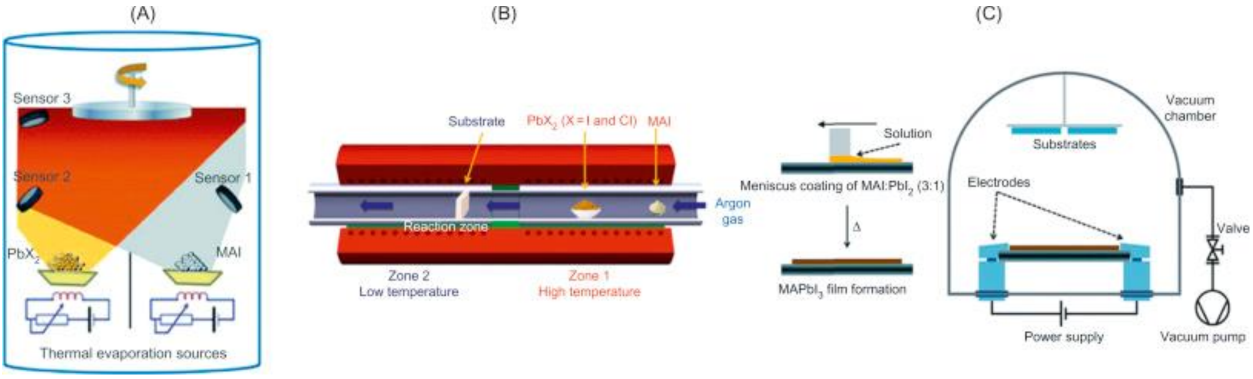

Figure I.12: Schematic images of (A) dual source evaporation, (B) chemical vapor deposition, and (C) flash evaporation [36].

Chapter II

Design of perovskite solar cell devices

Chapter II: Design of perovskite solar cell devices

II.1 Working principal of a perovskite solar cell

In a PSC, the perovskite layer is sandwiched between a p-type layer, also called HTM (Hole Transport Material), and a n-type layer, also called ETL (Electron Transport Layer), creating a p-i-n configuration. The success of perovskite as a solar absorber is largely dependent on the long charge diffusion length and high carrier mobilities in the medium. The electron and hole diffusion length in perovskite medium can reach as high as 1 μm which is large enough for the photogenerated charges to reach the interfacial layers and electrodes without geminate and non-geminate recombination, depending on the morphology of the perovskite medium [58].

There are two main device architectures known today in the preparation of perovskite solar cell, mesoporous-PSC and planar-PSC structures. Hence, the charge transport channels in PSC are often discussed in terms of the nature of these two device structures as shown below in **Figure II.1**

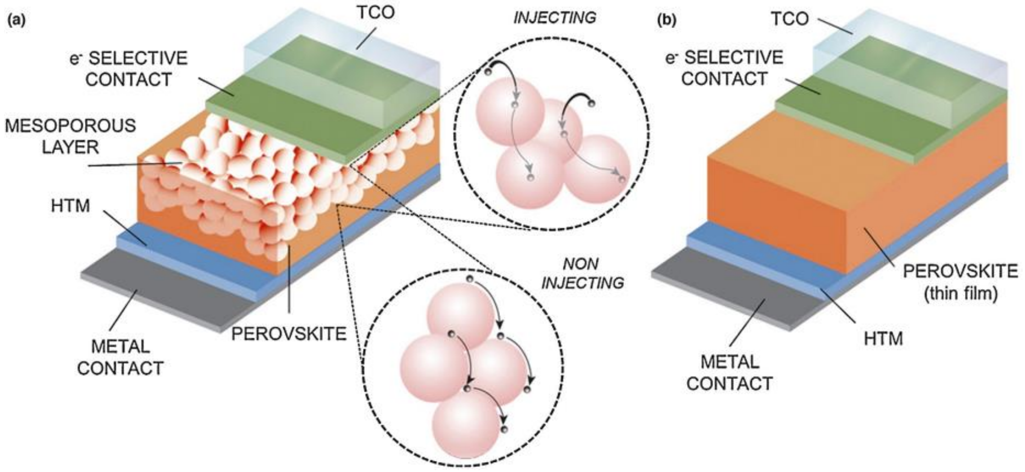

Figure II.1: Devices structure for (a) mesoporous perovskite solar cell structure and (b) structure of a thin film-like (planar) perovskite solar cell [59]**.**

In mesoporous structure, light is absorbed by the perovskite material, which leads to excitation of an electron from valence to conduction band of perovskite and the creation of an electron-hole pair. The charges dissociate readily thanks to the low exciton binding energy and they are free to move across the device. Electrons can either diffuse through perovskite to the mesoporous scaffold (if present and made out of suitable electron transport material such as TiO_2). Subsequently, electrons are collected at the electrode. Photogenerated holes diffuse through perovskite to reach HTL, from where they are collected at the metal electrode [60].

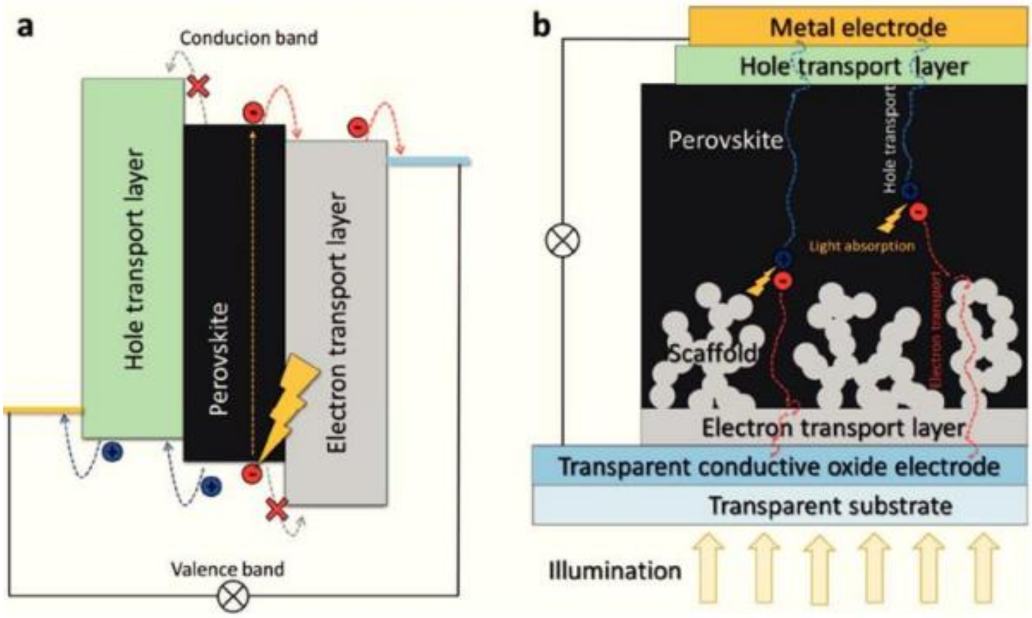

Figure II.2: Working principles of PSCs with (a) the schematic energy diagram of a PSC. (b) Schematics of the “normal” architecture PSC with mesoporous scaffold. Charge generation and transport processes are presented schematically [61]**.**

In the case of planar structure, the devices are fabricated using interfacial buffer layers of hole and electron transport material (ETM and HTM) through which the photo-generated charges created in the photoactive medium can be driven to the electrodes by the influence of either built in potential or external applied field.

II.2 Electrical outputs of a perovskite solar cell

II.2.1 Short Circuit Current (I_{SC})

For V = 0, only the short-circuit current (I_{SC}) flows through the solar cell. I_{SC} represents the maximum current that could be obtained in a solar cell. This current depends on the number of absorbed photons, surface area of the photo active layer, device thickness, and charge transport properties of active material, which play important role [62].

The equation for the short-circuit current can be approximated as [63]:

$$I_{SC} = -\,I_{ph} \tag{II.1}$$

I_{ph} : Photo-generated current by the solar generator under illumination (A)

II.2.2 Open Circuit Voltage (V_{OC})

The voltage at which no current flows through a solar cell is called open circuit voltage Voc and it is the maximum voltage available from solar cell. Several studies have demonstrated a strong dependence of Voc on the energy difference ΔE between the HOMO (highest occupied molecular orbital) of donor material and LUMO of acceptor material as in an organic solar cell [62].

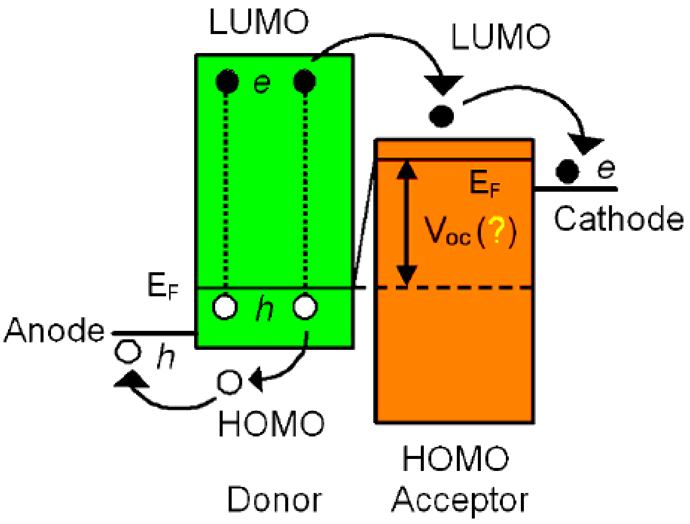

Figure II.3: Energy levels of D-A heterojunction organic solar cell [64].

II.2.3 Fill Factor (FF)

The FF, which determines the quality of solar cell can be obtained from the ratio of the maximum power output to the product of its V_{OC} and I_{SC} and is always < 1 [62]

$$FF = \frac{P_m}{I_{SC} \times V_{OC}} = \frac{V_m \times I_m}{I_{SC} \times V_{OC}} \tag{II.2}$$

Where :

P_m: Maximum power (W)

I_m: Maximum current (A)

V_m: Maximum voltage (V)

II.2.4 Photo-Conversion Efficiency (PCE)

It is a measure of the quality of the cell which provides evidence of how much power the cell will generate per incident photon. The PCE is the maximum electrical power P_{max} per light input P_L [62].

$$PCE = \frac{P_{max}}{P_L} \times (100\%) \tag{II.3}$$

$$P_L = E \times S \tag{II.4}$$

Where :

E : Intensity of illumination (w/cm^2) / S : The area of the solar cell

II.3 Evolution of the device architecture

Advances in the design of device architecture are one of the most important factors that drove the evolution of PSCs, especially in the early stage of the technical development. In 2009, PSCs were first demonstrated based on the design of the liquid electrolyte DSSC configuration. This device structure, inherited from the conventional DSSCs, has intrinsic material compatibility issues associated with the use of liquid electrolyte that limit the stability of the devices. Advances in solid-state HTM as a replacement for the liquid electrolyte led to the development of the mesoscopic and meso-super-structured architectures used in 2012. Based on these two preliminary structures, the so-called “regular” structure constructed with the HOIP (Hybrid Organic-Inorganic Perovskites) materials penetrating into a thin mesoporous metal oxide layer and forming a capping layer on the top was developed during 2013-2014. Since then, the regular structure has been widely used to fabricate high-efficiency PSCs. This success has attracted the experts of inorganic thin-films and organic PV materials to the field of PSC research, resulting in the development of the planar heterojunction structures in the n-i-p and p-i-n configurations. The planar p-i-n structure, with the film stack deposited in the opposite sequence of the regular structure, is often referred as the inverted structure [36].

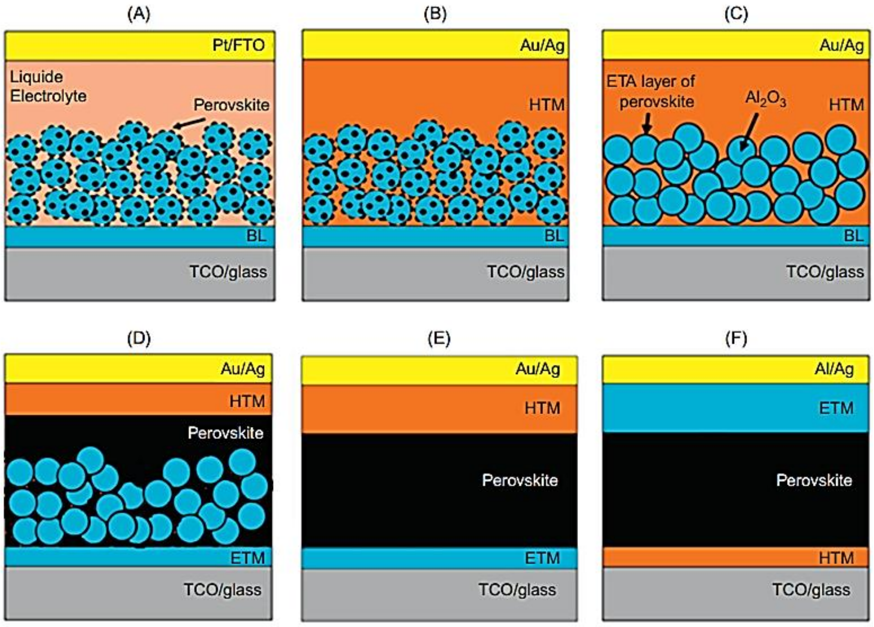

Figure II.4: Schematics of perovskite solar cell (PSC) architectures: (A) liquid electrolyte DSSC structure, (B) solid-state mesoscopic structure, (C) meso-superstructured structure, (D) the regular structure, (E) planar n-i-p heterojunction structure, and (F) planar p-i-n heterojunction structure (inverted planar structure). DSSC, dye-sensitized solar cells [36].

II.3.1 Liquid electrolyte DSSCs

PSCs were initially fabricated in the conventional DSSC structure which is comprised of a glass substrate/transparent conducting oxide (TCO), a thin compact TiO_2 (c-TiO_2) hole blocking layer, a several micron thick mesoporous TiO_2 (mp-TiO_2) layer sensitized with molecular dyes, a liquid electrolyte, and a counter electrode (Pt/TCO/ glass) [65].

Figure II.5 shows the conventional design of a DSSC with its working principle, which is based on photoexcitation of the sensitizer dye. When the incident photons are absorbed by the photosensitizers coating on the surface of TiO_2, electrons are excited from the ground state to the excited state. The photoexcitation results in the injection of electrons into the conduction band of mp-TiO_2, and then to the front electrode (anode). This process leaves the photosensitizers in an oxidized state, which is subsequently reduced back to the ground state by an injected electron from the reductants (e.g., I^-) in the liquid electrolyte. After the electron donation, the deactivated reductants, i.e., the oxidants (e.g., I^-_3), diffuse to the metal counter electrode and are regenerated by electrons from the cathode. This complete electron flow creates a photogenerated current in a DSSC.

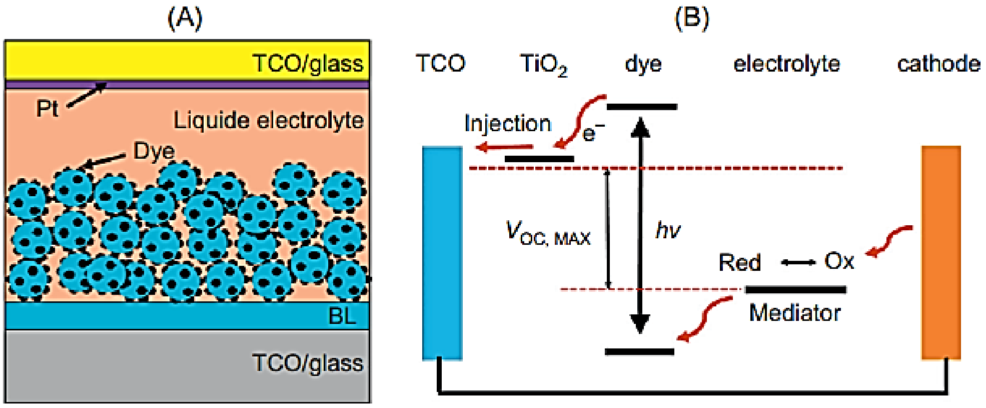

Figure II.5: (A) Schematic diagram and (B) working mechanism of the conventional DSSC. DSSC, dye-sensitized solar cells [36].

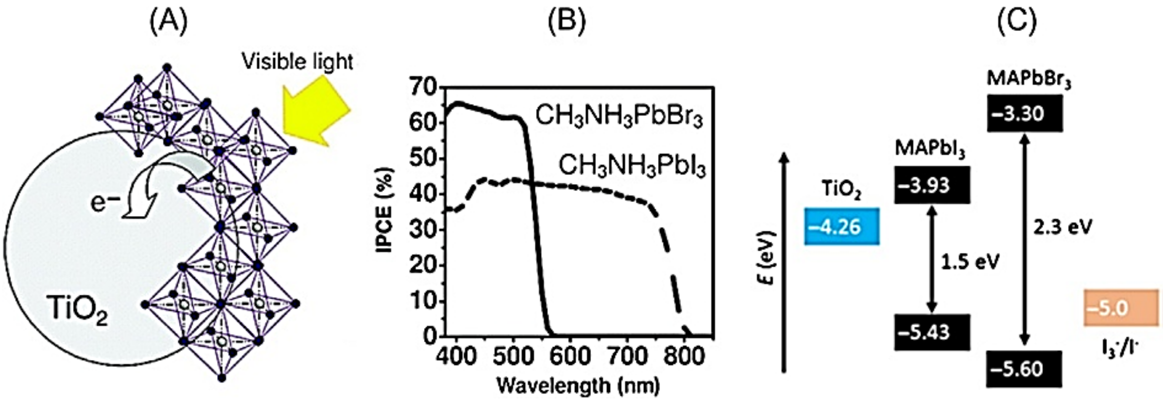

Figure II.6: (A) Schematic diagram of perovskite sensitizers. (B) IPCE of DSSCs using $MAPbI_3$ and $MAPbBr_3$. (C) Energy level diagram of a liquid-electrolyte DSSC with perovskite sensitizers [7].

The energy difference between the Fermi level of TiO_2 and the redox potential of the mediator in the electrolyte determines the maximum value of V_{OC} [27,65].

In 2009, Kojima et al. replaced the organic dye in the DSSC structure with $MAPbI_3$ or $MAPbBr_3$ perovskite (**Figure II.6A**) by spin-coating a precursor solution containing equimolar methylammonium and lead halide, MAX and PbX_2 (X = I or Br), onto the mp-TiO_2/c-TiO_2/fluorine-doped tin oxide (FTO) substrate [7]. The best $MAPbI_3$ device demonstrated a PCE of 3.8%, with an open circuit voltage (V_{OC}) of 0.61 V, a short circuit current density (J_{SC}) of 11.0 mA/cm^2, and a fill factor (FF) of 57%. In comparison, the champion $MAPbBr_3$ device had a PCE of 3.2%, with V_{OC} = 0.96 V, J_{SC} = 5.57 mA/cm^2, and FF = 59%. The higher J_{SC} of the $MAPbI_3$ device is a result of photoconversion of longer wavelengths light (550_800 nm) (**Figure II.6B**) due to a lower bandgap (1.5 eV) relative to $MAPbBr_3$ (2.3 eV), but the V_{OC} of the $MAPbI_3$ devices is lower due to a smaller energy level difference between the conduction band of the perovskite absorber and the redox potential of the X^{3-}/X^- (X = I or Br) mediator (**Figure II.6C**). Although this work demonstrated the potential of using the HOIP materials in PV applications, it did not receive much attention due to the relatively low efficiency and instability of the devices.

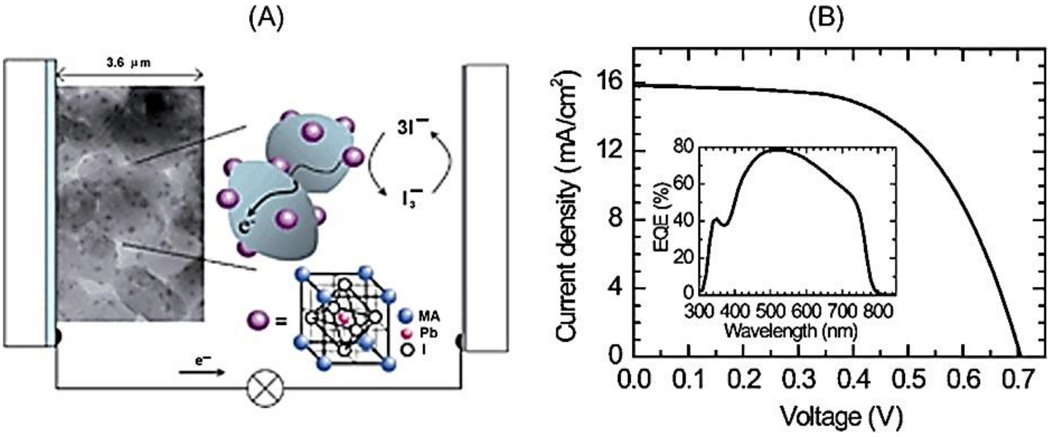

Figure II.7: (A) Schematic of a dye-sensitized solar cells (DSSC) with the perovskite quantum dots (QDs). (B) Current density-voltage (J-V) and external quantum efficiency (EQE) curves of the devic [27].

Two years later, Im et al. fabricated perovskite-sensitized DSSCs using 2-3 nm $MAPbI_3$ quantum dots (QDs) to coat the 3.6 μm thick mp- TiO_2 layer (**Figure II.7A**) [12]. Their champion device shows an improved PCE of 6.54%, with V_{OC} = 0.706 V, J_{SC} = 15.82 mA/cm^2, and FF=58.6% (**Figure II.7B**). The J_{SC} enhancement is due to the improved light conversion in the $MAPbI_3$ QDs, which shows the maximum external quantum efficiency of ~80% at 530 nm. The increased V_{OC} is likely due to the thicker mp-TiO_2 that prevents recombination at the perovskite/FTO interface. Watthage et al. [36] revealed the high light absorption coefficient of the HOIP materials, which is one of the key factors for fabricating high-efficiency solar cells. Still, instability of these devices limits their practical application—the device performance degraded ~ 80% in 10 min due to the dissolution of the perovskite QDs in the liquid electrolyte.

II.3.2 Solid-State mesoscopic structure

To overcome the instability issue associated with the liquid electrolyte, Kim et al. in 2012 developed the first solid-state PSC by replacing the liquid electrolyte with the solid HTM 2,2’,7,7’-tetrakis-(N,N-di-p-methoxyphenyl-amine)-9,9’-spirobifluorene (Spiro-MeOTAD) that was successfully used in solid-state DSSC [28].

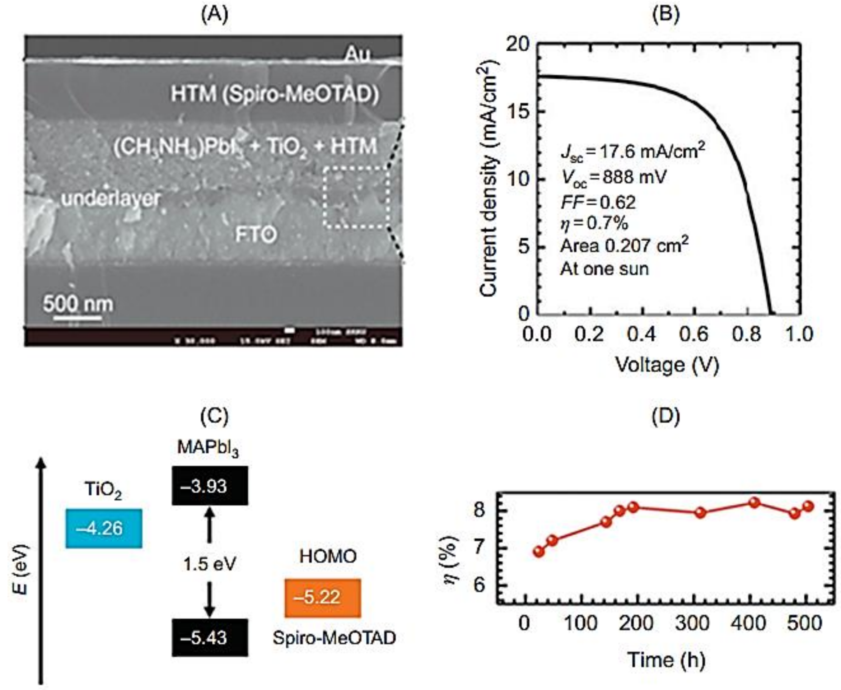

Figure II.8: (A) Cross-sectional scanning electron microscope (SEM) image, (B) J-V characteristic, (C) energy level diagram, and (D) stability of a perovskite solar cell (PSC) in solid-state mesoscopic structure [28].

This device configuration was named the mesoscopic structure because it consists of a thin mp-TiO_2 layer similar to that used in the liquid electrolyte perovskite-sensitized solar cells, although the thickness of the mp-TiO_2 layer was reduced from ~3 to ~0.6 µm. In this device configuration, part of the Spiro-MeOTAD HTM penetrates into the pores of the mp-TiO_2 layer, making direct contact with the perovskite sensitizers. The remaining HTM material forms a dense capping layer that covers the mp-TiO_2, preventing shunts between the electron transport materials (ETMs) and the back contact (**Figure II.8A**) .

The mesoporous architecture in perovskite is actually derived from the DSSC, where TiO_2 is used as a mesoporous layer and the sensitizer occupies the pores of m-TiO_2 [66]**.**

The working principle of this device configuration differs from the conventional DSSCs. In contrast to the electrolyte that suffered from low charge carrier mobility, the solid-state Spiro-OMeTAD allows holes to move more efficiently. The champion device demonstrated a PCE of 9.7%, with V_{OC} = 0.89 V, J_{SC} = 17.6 mA/cm^2, and FF = 62% (**Figure II.8B**). Replacing the liquid electrolyte with the solid HTM significantly improved V_{OC} from 0.71 to 0.89 V due to the better alignment of the highest occupied molecular orbital (HOMO) level of the Spiro-MeOTAD (-5.22 eV) with the valance band of $MAPbI_3$ (- 5.43 eV), enabling more efficient hole extraction from the perovskite absorber and widening the hole Fermi energy splitting under illumination (**Figure II.8C**). In addition to the PCE improvement, the device stability was also dramatically enhanced. Some devices even exhibited the enhanced PCEs after 500 h of operation (**Figure II.8D**).

II.3.3 Meso-super-structured structure

Analogous to the mesoscopic configuration, Snaith et al. invented the meso-super-structured structure by replacing the mp-TiO_2 layer with the insulating Al_2O_3 [67]**.** This device configuration has almost the same structure as in the mesoscopic structure (**Figure II.9A**) but the perovskite materials formed a continuous extremely thin absorber (ETA) layer on the surface of the porous metal oxide (**Figure II.9B**). Leijtens et al. investigated a mixed halide $CH_3NH_3PbI_{3-x}Cl_x$, instead of the pure $MAPbI_3$ perovskite as the absorber material, and studied the electronic properties of the meso-superstructured perovskite films [68].

The champion device with the porous Al_2O_3 layer achieved a PCE of 10.9%, with V_{OC} = 0.98 V, J_{SC} = 17.8 mA/cm^2, and FF = 63%, while the best control device made with mp-TiO_2 demonstrated a PCE of 7.6% with V_{OC} = 0.80 V, J_{SC} = 17.8 mA/cm^2 ,and FF = 53%. Interestingly, a significantly higher V_{OC} value of ~1.1 V was achieved in some devices with the Al_2O_3 layer. This low V_{OC} deficiency, i.e., the difference between Eg/e of the absorber material and V_{OC} of the corresponding devices, indicates low nonradiative recombination and long carrier diffusion lengths of the mixed halide perovskites. These excellent optoelectronic properties that favor the PV application were confirmed by optical and charge transport measurements [11,69].

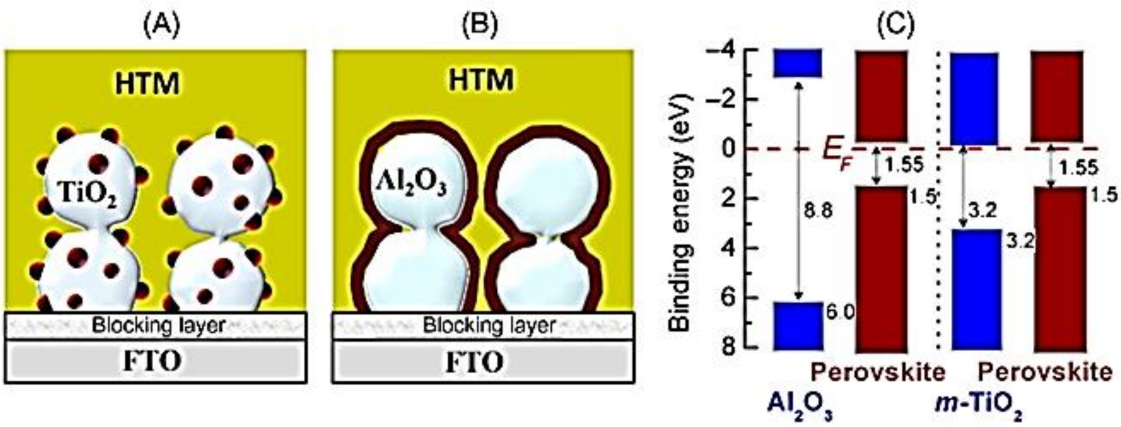

Figure II.9: Schematic diagram of (A) mesoporous and (B) meso-superstructured perovskite solar cells (PSCs). (C) Measured binding energy of perovskite, Al_2O_3/perovskite, and mp-TiO_2/perovskite [68,70].

II.3.4 The regular structure

The regular device structure was originated from the PSCs with “pillared structures.” In 2013, Heo et al. reported this structure with $MAPbI_3$ completely filled the pores of the mp-TiO_2 and formed individual $MAPbI_3$ pillars (**Figure II.10A**) [71]**.** These perovskite pillars were covered by a thin polytriarylamine (PTAA) HTM and Au electrode to complete the device. The PCE of the best cell was 12%, with V_{OC} = 0.997 V, J_{SC} = 16.5 mA/cm^2, and FF = 72.7%. Heo et al. found that devices that had a mp-TiO_2 layer of ~600 nm exhibited the best incident photon-to-electron conversion efficiency (**Figure II.10B**) and device performance (**Figure II.10C**) due to the formation of a perovskite overlayer. However, this overlayer suffered from a rough and discontinuous morphology, limiting the improvement of device performance [36]**.**

The further progress of the regular structure was propelled by the advances in the perovskite film deposition techniques [56], allowing thicker perovskite films to be deposited on a thinner mp-TiO_2 layer. Burschka et al. reported PSCs with the best PCE of 15% in the regular configuration by fabricating a smooth and thin perovskite capping layer (~50 nm) on the top of a ~300 nm mp-TiO_2 layer (**Figure II.11A**) using the two-step sequential deposition method [72].

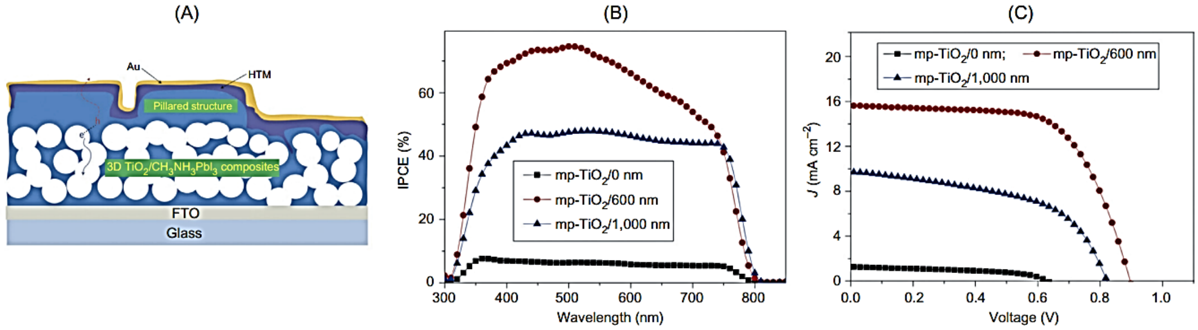

Figure II.10: (A) Schematic illustration, (B) Incident photon-to-electron conversion efficiency (IPCE) curves, and (C) J-V characteristics of the perovskite solarcells (PSCs) withdifferent mp-TiO_2thickness [71].

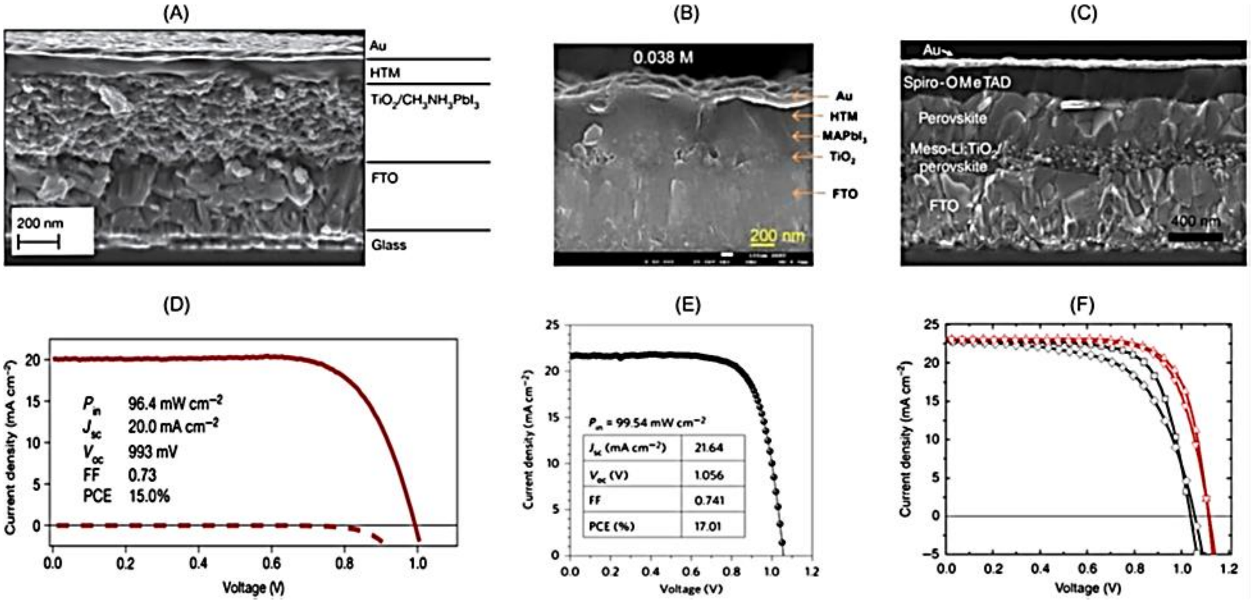

Figure II.11: (A–C) Cross-sectional scanning electron microscope (SEM) imag and (D–F) corresponding J–V curves of perovskite solar cell (PSCs) with different perovskite capping layer [72–74].

The efficiency enhancement, especially the improved J_{SC} (20.0 mA/cm^2) (**Figure II.11D**), was mainly due to the formation of a dense and uniform perovskite layer. The same deposition technique was then used by Im et al. to prepare PSCs on a thinner mp-TiO_2 layer (~100 nm), resulting in the increased thickness of the perovskite capping layer (~150 nm) (**Figure II.11B**) [73], and improved the J_{SC} (21.64 mA/cm^2), V_{OC} (1.056 V), and efficiency (17%) of the devices (**Figure II.11E**). By employing the Li-doped TiO_2 and a thicker perovskite capping layer (~ 300 nm) (**Figure II.11C**), Giordano et al. achieved a PCE of 19.3%, with V_{OC} = 1.114 V, J_{SC} = 23.0 mA/cm^2, and FF = 74% (**Figuer II.11F**) [74]. To date, the state-of-the-art PSCs with PCEs >20% were predominantly fabricated in the regular configuration [56].

II.3.5 Planar n-i-p hetero-junction structure

The planar structure does not contain a mesoporous scaffold; the advantage of the mesoporous layer is a low-temperature processing route, which gives it better flexibility for its use in tandem solar cells and flexible substrates. It also opens the space for using different synthesis routes and interfacial engineering for better performing devices [75]**.** The standards of the film are one of the key challenges as it, in turn, determines various factors, such as charge transport, charge dissociation, and diffusion length [69,76]**.**

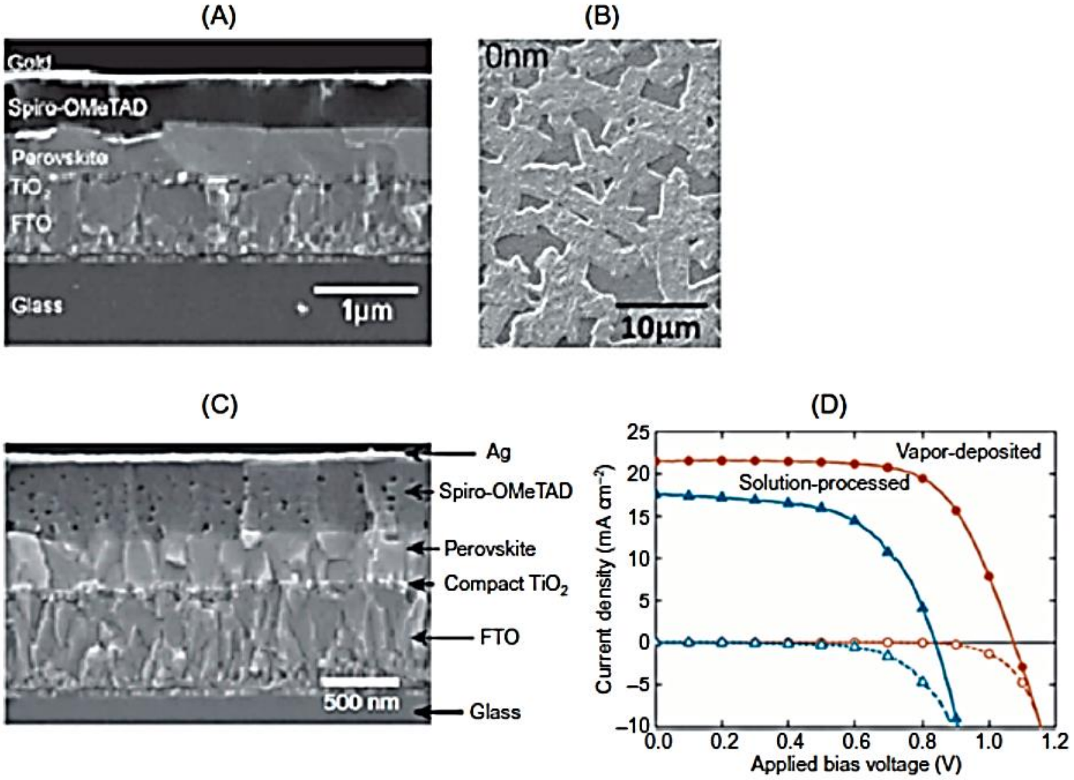

Figure II.12: (A) Cross-sectional and (B) surface SEM images of a PSC in the planar n-i-p configuration prepared by solution-based deposition. (C) Cross-sectional scanning electron microscope (SEM) image of a perovskite solar cells (PCSs) prepared by the vapor-based deposition. (D) J-V characteristics of the planar n-i-p type PSCs [57,76].

The planar n-i-p heterojunction structure (**Figure II.4E**) was developed as the mesoporous oxide layer of the regular structure gets thinner that they eventually were removed. Analogous to inorganic thin-film solar cells, the structure is comprised of a TCO cathode, an n-type ETM, an intrinsic perovskite layer, a p-type HTM, and a metal anode. Due to the low exciton bounding energy and long diffusion lengths of charge carriers, photoexcited electrons and holes have sufficiently long lifetimes to transport to the interfaces with the charge selective layers (HTM and ETM). In 2012, Snaith et al. made the first attempt on planar heterojunction PSCs using $MAPbI_{3-X}Cl_X$ but only achieved a PCE of 1.8% [67], likely due to the incomplete film coverage that led to shunts in the devices. Efforts to increase the PCE by optimizing the processing conditions, including annealing temperature and film thicknesses, resulted in the values of 4.5% [77] in 2013 and 11.4% [76] in 2014.

The champion device achieved a PCE of 15%, with V_{OC} = 1.07 V, J_{SC} = 21.5 mA/cm^2, and FF = 0.67 (**Figure II.12D**). Thanks to the advances in the film deposition techniques, the present state-of-the-art planar PSCs prepared bysolution-based deposition methods yields PCEs of ~20% [78–80], with a V_{OC} of up to 1.214 V [80]. Additionally, these devices exhibit edstable performance under operating conditions over hundreds of hours [81]. These advancements in efficiency and stability have made the planardevice structure a promising candidate for the commercialized manufacturing of PSCs.

II.3.6 Inverted planar p-i-n hetrojunction structure

While the regular and planar n-i-p structures progressed, the planar p-i-n heterojunction structure originally used in the organic PV devices was adopted by the PSC community as an alternative. Because the planar p-i-n heterojunction structure has an opposite sequence of HTM and ETM than the regular configuration, it is often referred as the "inverted" structure (**Figure II.4F**). The p-i-n structure is comprised of a TCO anode, a p-type HTM, an intrinsic perovskite layer, an n-type ETM, and a metal cathode. In 2013, Jeng et al. reported the prototype of planar p-i-n PSC with the structure indium tin oxide (ITO)/PEDOT:PSS/$MAPbI_3$/C_{60}/bathocuproine (BCP)/Al [82], where they categorized the $MAPbI_3$/C_{60} as a planar heterojunction and BCP and polypolystyrene sulfonate (PEDOT:PSS) as the ETM and HTM (**Figure II.13A**). The preliminary device yielded a PCE of 1.6%, which improved to 3.9% when phenyl-C_{61}-butyric acid methyl ester ($PC_{61}BM$) was used instead of C_{60}. The increased efficiency was attributed to the larger energy offset between the HOMO of $MAPbI_3$ (donor) and the lowest unoccupied molecular orbital of $PC_{61}BM$ (acceptor) and more efficient electron injection into the Al cathode (**Figure II.13B**).

The efficiency of PSCs in the planar p-i-n structure has rapidly progressed. Sun et al. applied the solution-processed $PC_{61}BM$ to the p-i-n type PSC and improved the PCE to 7.4% [83]. Snaith et al. prepared the planar PSC in the structure FTO/PEDOT:PSS/$MAPbI_{3-X}Cl_X$/$PC_{61}BM$/TiO_X/Al and obtained a PCE of 9.8% [84]. You et al. further improved the device efficiency to 11.5% by optimizing the perovskite deposition [85]. Malinkiewicz et al. employed the coevaporation technique for preparing $MAPbI_3$ and achieved a 12.0% PCE champion cell [86]. Wang et al. introduced a double fullerene layer consisting of C_{60} and $PC_{61}BM$ to passivate the perovskite film [87] and demonstrated a 12.2% PCE device with a record high FF of 80.1%.

The champion obtained PCE was 19.5%, with J_{SC} = 22.6 mA/cm^2, V_{OC} = 1.07 V, and FF = 80.6% [88].

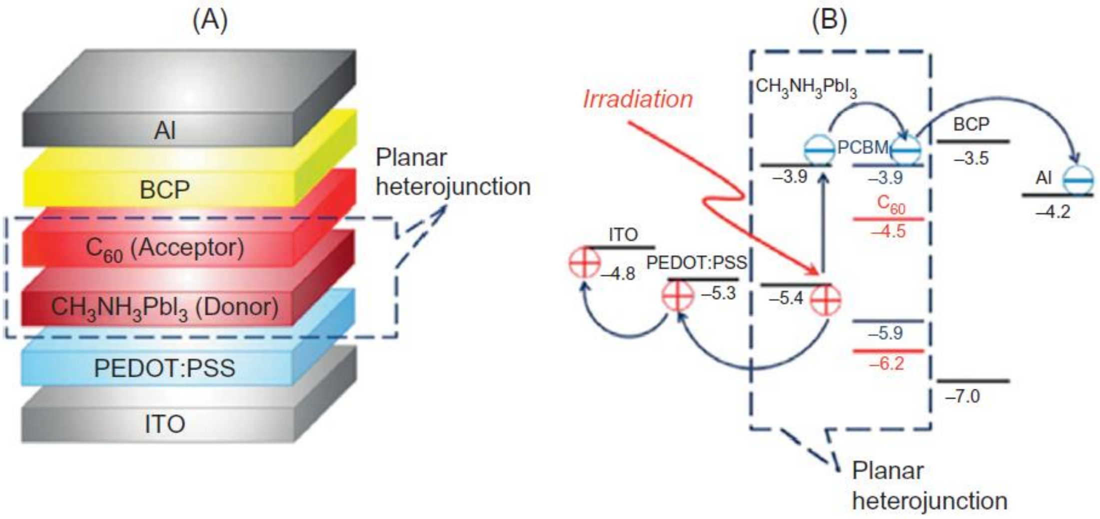

Figure II.13: (A) Structure and (B) energy level diagram of a perovskite solar cell (PSC) in the planar p-i-n heterojunction structure [82] .

II.4 Advanced device engineering techniques

The rapid progress of PSCs in the early stage (2012-14) relied mainly on the innovation on the device architecture and film preparation method. During this period, the champion PCE was rapidly increased to 15%. The further advances in fabricating high-efficiency PSCs with PCEs of ~ 20% were enabled by some advanced device engineering techniques developed in 2014-16 to address problems associated with the primary deposition methods and improve the quality of the perovskite films [56]. These strategies, solvent engineering, deposition process engineering, contact material engineering, and band-gap engineering, yield uniform and dense perovskite films with improved optoelectronic properties and interface passivation. Consequently, the present state-of-the-art PSCs typically employed combined engineering strategies to achieve high performance and stability. In addition to single junction PSCs, research on perovskite-based tandem devices has been progressed as a promising future direction [36].

II.4.1 Contact materials engineering

Various materials possessing combined merits, including proper band alignment with the conduction or valence band of the perovskite absorber, efficient charge carrier transport, and low charge recombination defect densities at the interfaces, have been developed as the ETMs or HTMs. (**Figure II.14)** shows the band energy levels of these commonly used ETM and HTM in comparison with HOIPs and electrodes [56].

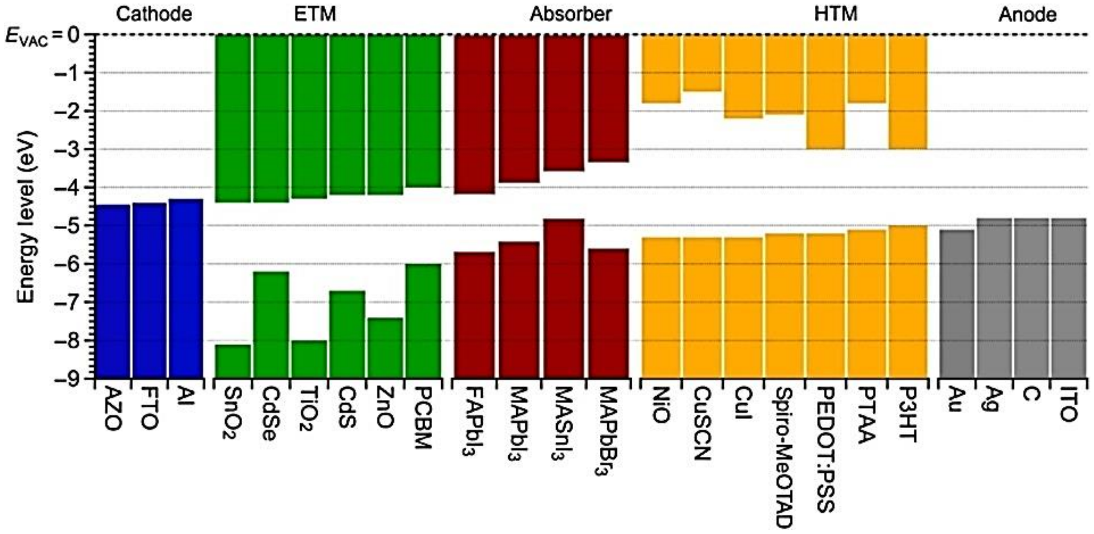

Figure II.14: Energy levels of commonly used cathode, n-type (ETM), absorber, p-type (HTM), and anode materials in perovskite solar cells, ETM, electron transport materials; HTM, hole transport material [56] .

Since the PSCs emerged, TiO_2 has been widely used as the compact and porous ETM in the p-i-n structure configuration [7,27]. With the evolution of perovskite technology, the thickness of the mp-TiO_2 layer, conventionally used in DSSCs, gradually decreased from ~4 µm to ~100 nm in the regular structure and was omitted in the planar structure [57,73,76]. This progress was enabled by the high crystallinity and long carrier lifetime of the HOIP materials. Removing the mesoporous oxide layer made the compact ETM an essential component of the devices for efficient collection of photoexcited electrons. Besides c-TiO_2, other ETMs such as ZnO [89], SnO_2 [78–80,90,91], CdSe [92], CdS [93], TiO_2-graphene [87], and yttrium-doped TiO_2 [58] have been developed as ETMs. The use of these alternative ETMs allows PSCs to be processed without high temperature (~500°C) treatment that is required for the anatase TiO_2 [36].

C_{60} and its derivatives such $PC_{61}BM$ or $PC_{71}BM$ are among the commonly used organic ETM materials in the p-i-n device configuration [83,94]. These materials can also be processed at low temperatures, enabling the potential for roll-to-roll manufacturing on flexible substrates and incorporating with another cell to fabricate tandem devices [36].

HTMs are also critical for a good PV performance, especially for a high V_{OC} [95]. Both organic and inorganic HTMs have been investigated in recent years. The organic HTMs can be categorized into two groups: small molecules and conducting polymers. Spiro-MeOTAD is the most used small molecules HTM due to high device performance (>20% PCEs) [96]. However, the devices using spiro-OMeTAD typically exhibit poor stability, especially after exposure to humidity [97–99]. Conducting polymers of PTAA, P3HT [Poly(3-hexylthiophene-2,5-diyl)], and triazatruxene derivatives have also been applied as the HTMs [100]. Among them, PTAA (20.2%) [101] and triazatruxene derivatives (18.3%) [102] showed competitive PCEs to the Spiro-MeOTAD but improved stability. P3HT, on the other hand, is not good as the Spiro-OMeTAD, demonstrating only 12% - 15% efficiencies [100,103]. Nonetheless, higher material cost and lack of stability of the organic HTMs are still the main hurdles for the commercialization of PSCs. One possible solution is employing cost-effective and more stable inorganic HTMs, such as NiO_X [104–107], CuO [108], Cu_2O [108], and CuSCN [109]. Among these, the devices using NiO_X showed >17% PCE [106,107], which is promising for utilization in commercial manufacturing.

II.4.2 Band-gab engineering of perovskite

In the early stage of PSC progress (2009_2013), $MAPbI_3$ was used as the prototype due to its bandgap of 1.55 eV that is suitable for highe fficiency solar conversion [7,28]. As the field advanced, the composition of the perovskite AMX_3 has been altered by incorporating other monovalent cations A [formamidinium (FA^+) and Cs^+], divalent cation M (Sn^{2+}), and halide ions X (Br^- and Cl^-), which results in optical absorption tunability (**Figure II.15)** [10,110]. This versatility in optical bandgap enables various PV applications of PSCs, including single junction devices as well as both the top and bottom cells in tandem structures [111].

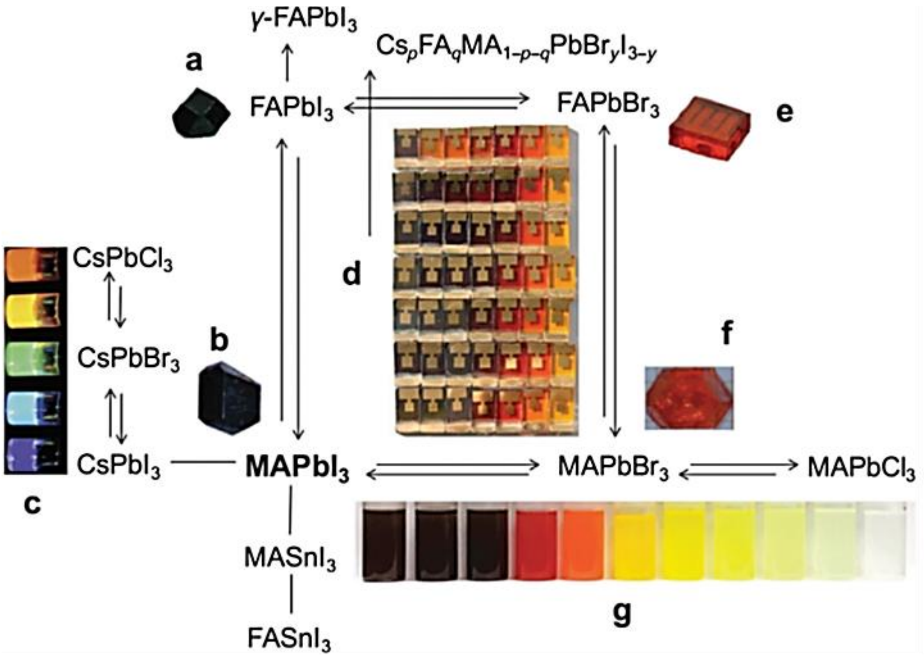

Figure II.15: The versatility of hybrid perovskite materials $Cs_pFA_qMA_{1-p-q}PbBr_yI_{3-y}$ and their absorption tunability [110].

The substitution of different halide anions X can be used to tune the optical bandgap of the metal halide perovskites (**Figure II.15**). $MAPb(I_{1-X}Br_X)_3$ is commonly used to fabricate high bandgap perovskite absorber layer [112–114]. Increasing Br content (x value) results in a continuous blue (gray in print versions) shift of the absorption band edge from 1.5 eV (830 nm) at x = 0 to 2.3 eV (540 nm) at x = 1 (**Figure II.16A)** [113–115]. In contrast to Br incorporation, which is used to alter the bandgap, the Cl mixed phase $MAPb(I_{1-X}Cl_X)_3$ shows negligible bandgap alternation to the pristine $MAPbI_3$ (**Figure II.16B**) due to the relatively low Cl concentrations (<4%) in the final product [67]. However, the charge carrier diffusion length in $MAPb(I_{1-X}Cl_X)_3$ is greater than 1 μm, which is one order of magnitude higher than the pure iodide perovskite [11], leading to the improved PV performance. Therefore, $MAPb(I_{1-X}Cl_X)_3$ was widely used to fabricate high-performance devices in the early stage (2012_2014) [67,115–117]. To date, perovskite absorbers combined mixed organic cations (FA^+ and MA^+) and halides (I^- and Br^-) have been widely used to fabricate $FA_{1-X}MA_XPb(I_{1-Y}Br_Y)_3$ based solar cells [60], which has achieved >20% PCE with a high degree of reproducibility [96,118]. The present champion PSC with the $FA_{1-X}MA_XPb(I_{1-Y}Br_Y)_3$ absorber demonstrated a PCE of 22.1%, with V_{OC} = 1.105, J_{SC} =24.97 mA/cm^2, and FF = 80.3% [101].

The substitution of divalent cation M can also alter the bandgap of the perovskite absorber. Due to the environmental concerns with watersoluble lead based perovskites [119,120], many research efforts have been devoted to replacing Pb by nontoxic Sn [121,122]. The $MASnI_3$ perovskite has a lower bandgap (~1.2 eV) compared to its Pb counterpart (1.55 eV) and thus exhibits light absorption at the longer wavelengths, which is beneficial for a higher J_{SC} [10]. However, due to the high V_{OC} deficit, the pure Sn-based PSCs typically exhibited poor PV performance [121,123]. More recently, mixed tin_lead perovskite low-bandgap PSCs have been developed for bottom-cell tandem solar cells [124,125]. Recently, Zhao et al. achieved a 17.6% PCE, with V_{OC} =0.853 V, J_{SC} =28.5 mA/cm^2, and FF = 72.5% in a single junction PSC based on $(FASnI_3)_{0.6}(MAPbI_3)_{0.4}$ perovskite film [125]. Further, by connecting this with a ~1.58 eV bandgap perovskite top cell, they were able to achieve a steady-state efficiency of 21.0% in the four-terminal tandem cell.

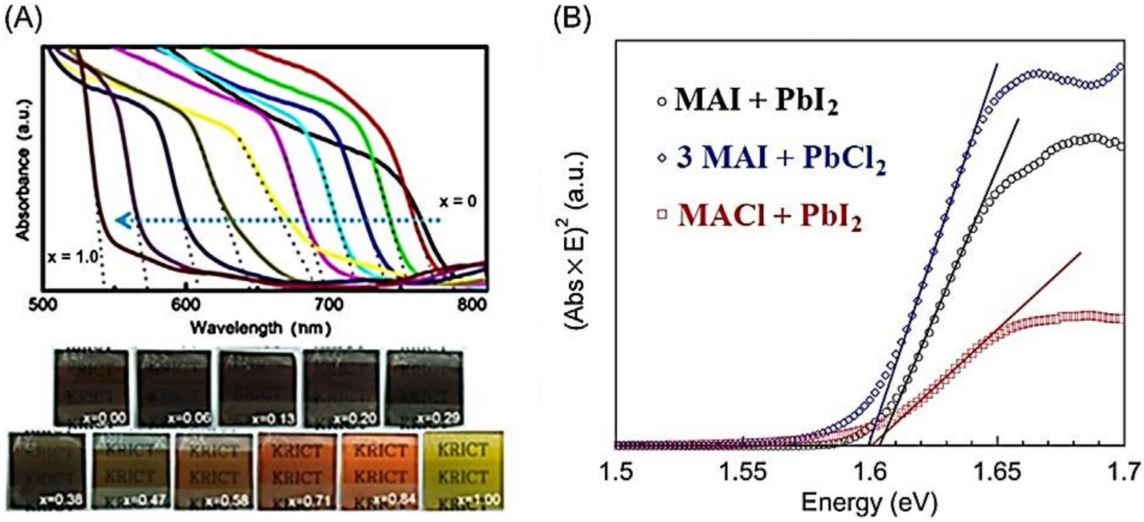

Figure II.16: (A) Photographs and UV-VIS absorption spectra of $MAPb(I_{1-x}Br_3)_3$. (B) UV- vis spectra of $MAPb(I_{1-x}Cl_x)_3$ [114,116].

II.4.3 Sn–Pb-Based Lead-Less PSCs

Lead-less solar cells based on tin are recent. The first study of Sn-based hybrid halide perovskite was carried out in 1974 by Fischer et al. who made and characterized $CsSnX_3$ with X being Cl, Br, and I [1]. Later, different groups pursued the investigation of those materials to determine their nature, even with dimension reduction until it was verified that they are indeed semiconductors [1]. In the 1990 decade, Mitzi et al. conducted a lot of pioneering researches on Sn-based perovskites and Sn-based hybrid halide compounds being well-defined; they were first used in photovoltaic devices in 2012 [1]. The Sn-based perovskite was then used as a HTL and absorbing material in an all-solid-state DSSC [1]. Later, it was revealed that $MASnI_3$ and $FASnI_3$ perovskites could be good candidates as light absorber materials thanks to their electronic and optical properties such as carrier mobilities, tunable direct-bandgap, strong photoluminescence in the same way than their lead peers [1]. The first reports on Sn-based PSCs were published, unveiling $MASnI_3$ and $MASnIBr_2$ devices reaching PCEs of 5.23% and 5.73%, respectively [1].

In addition, according to the theoretical study by Mandadapu et al. published in 2017, $MASnI_3$ PSCs with a ZnO:Al/TiO2/$MASnI_3$/ CuI/Au normal planar architecture have the potential to reach a theoretical maximum efficiency of 24.82% thus encouraging the community to overcome the current bottlenecks and to achieve higher efficiencies [1]. **Figure II.17** shows other possible elements that can be used to replace partially Pb [1].

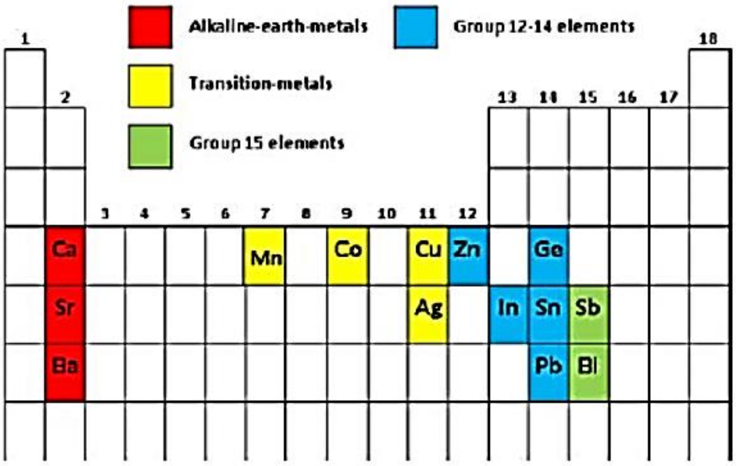

Figure II.17: Elements reported in [1] to substitute Pb in lead-less PSCs.

Recently, in 2020 it was reported that halogen substitutions have effect on the properties of $MASn_{0.5}Pb_{0.5}I_{3-y}X_y$ (X=Br or Cl) perovskites and based on density functional theory (DFT) they enlarges the bandgap [1]. Finally and based on the mentioned properties and results in [1], Sn–Pb lead-less PSCs are good candidates to equalize classical Pb-based PSCs while reducing lead content in the meantime.

Chapter III

Study of MAPbSn(Cl/I) perovskite solar cell by Silvaco-Atlas

Chapter III: Study of MAPbSn(Cl/I) perovskite solar cell by Silvaco-Atlas

III.1 Introduction

By physical process simulation, we mean the use of mathematical description, or model, of a real system in the form of a computer program. This model is composed of equations that duplicate the functional relationships within the real system. A numerical method is a tool that enables the prediction of the behavior of the system from a set of parameters and initial conditions and allows us to achieve results not achievable by other means [126].

Numerical simulation is also a powerful way to analyze, predict, interpret and understand the physical phenomena governing the transport in devices such as solar cells. In addition, the study of the real behavior of solar cells requires a detailed description of the device to simulate and materials used in its realization. The selection of the type of material and its composition as well as its electrical and physical properties are very important and directly affect cell performance [126].

The objective of this chapter is to describe the simulation software SILVACO-ATLAS and its implementation in the framework for Investigation of the electrical characteristics and the photo-parameters of the perovskite-based solar cell by considering its related structure configurations.

III.2 Importance of modeling

There are a very large number of publications available that document the modeling of almost every aspect of solar cell function and behavior. These span from the macroscopic electrical to the microscopic molecular level and have very high accuracy and credibility. However, they all address individual solar cell viewpoints, without providing complete coverage of the complex combination of phenomena that actually take place. Thus, there is a need to select and use a large number of different models, in order to study an actual complete cell structure. An important consideration is a fact that not all of these models are compatible with each other. This makes their selection prone to errors, quite hard, and time consuming. In addition, each one exposes the researcher to many detailed parameters that usually create a lot of unnecessary confusion. All the above make a complete simulation of advanced solar cells a hard task [126].

As a consequence, solar cell research today is conducted by actually fabricating cells and experimenting with them. Then, researchers theorize about the collected results. Although that methodology provides the most credible results, it may also lead to some confusion. The reason lies in the huge number of factors that always need to be considered, most of which are more relevant to the fabrication process used and not the cell itself. Therefore, many combinations of parameters need to be materialized like material types and characteristics, doping, dimensions, fabrication conditions, and processes. This is not only time and personnel consuming task, but can also be expensive to carry out. The number of experiments, needed to answer questions, is also very large because experts are not allowed to focus on a certain issue. Instead, they need to consider and develop the design and the complete fabrication process of the cell under study. Additionally, in any kind of experiment, there is always a number of unpredictable factors that may introduce deviation among results [126].

III.3 Silvaco-Atlas

SILVACO (Silicon Valley Corporation) is an American international company that specializes in the creation of simulation software headquartered in Santa Clara, California. This company is one of the leading suppliers of channels finite element simulation software and design-assisted computer for electronics technology TCAD (Technology Computer Aided Design) targeting almost every aspect of modern electronic design [127].

Atlas is a software environment to design and predict the performance of semiconductor devices, which can be modeled in either two dimensions (2D) or three dimensions (3D). Atlas can accept structure description files from Athena and Devedit, but also from its own command files, the development of the desired structure in Atlas is done using a declarative programming language. This is interpreted by the Atlas simulation engine to produce results [127].

The first line to be read by the program when running ATLAS using DeckBuild is the GO ATLAS command. After that, the structure of the statement should be followed in the sequence depicted in **Figure III.1** if the order is not respected, an error message appears and the program does not execute correctly. An ATLAS statement is comprised of a keyword and a set of parameters, which are not case sensitive, in the following format [127]:

<STATEMENT> <PARAMETER>=<VALUE>.

A brief walk–through of how a structure is built and simulated follows.

III.3.1 Mesh

The grid consists of horizontal and vertical lines with a user-defined distance between them. It bounds the physical area of the cell by creating a number of triangles in which the simulation will take place [127].

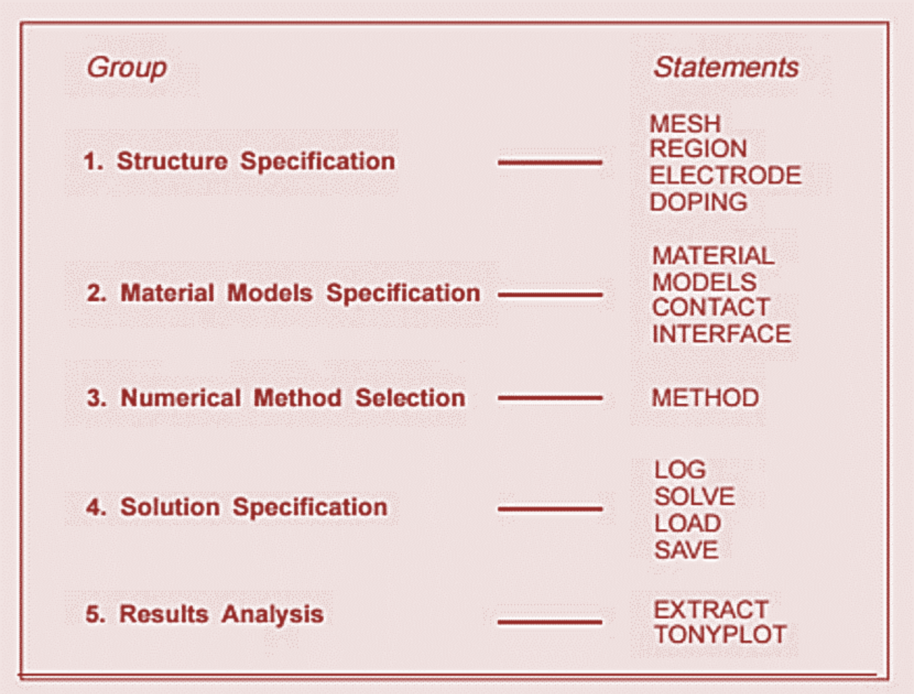

Group	Statements
1. Structure Specification	MESH REGION ELECTRODE DOPING
2. Material Models Specification	MATERIAL MODELS CONTACT INTERFACE
3. Numerical Method Selection	METHOD
4. Solution Specification	LOG SOLVE LOAD SAVE
5. Results Analysis	EXTRACT TONYPLOT

Figure III.1: Command group and statements layout for a Silvaco Atlas file [127].

The first thing that needs to be specified is the mesh on which the device will be constructed this can be 2D or 3D and can be comprised of many different sections. Orthogonal and cylindrical coordinate systems are available. Several constant or variable densities can be specified while scaling and automatic mesh relaxation can also be used. This way, a number of minimum triangles are created; this determines the resolution of the simulation. The correct specification of the mesh is very important for the final accuracy of the results. If the number or density of triangles is not high, enough in regions, such as junctions or material boundaries, the results of the simulation will be crude and possibly misleading. On the other hand, the use of too many triangles will likely lead to significant and unnecessary increases in execution time, So a fine defined mesh will lead to more accurate results, and on the other hand, a coarse mesh that minimizes the total number of grid points will lead to a larger numerical efficiency [127].

An example of both fine and coarse meshes designed in ATLAS is depicted in **Figure III.2**

III.3.2 Region

The next step in creating a semiconductor device is to separate the created mesh into regions. The format to define the regions is:

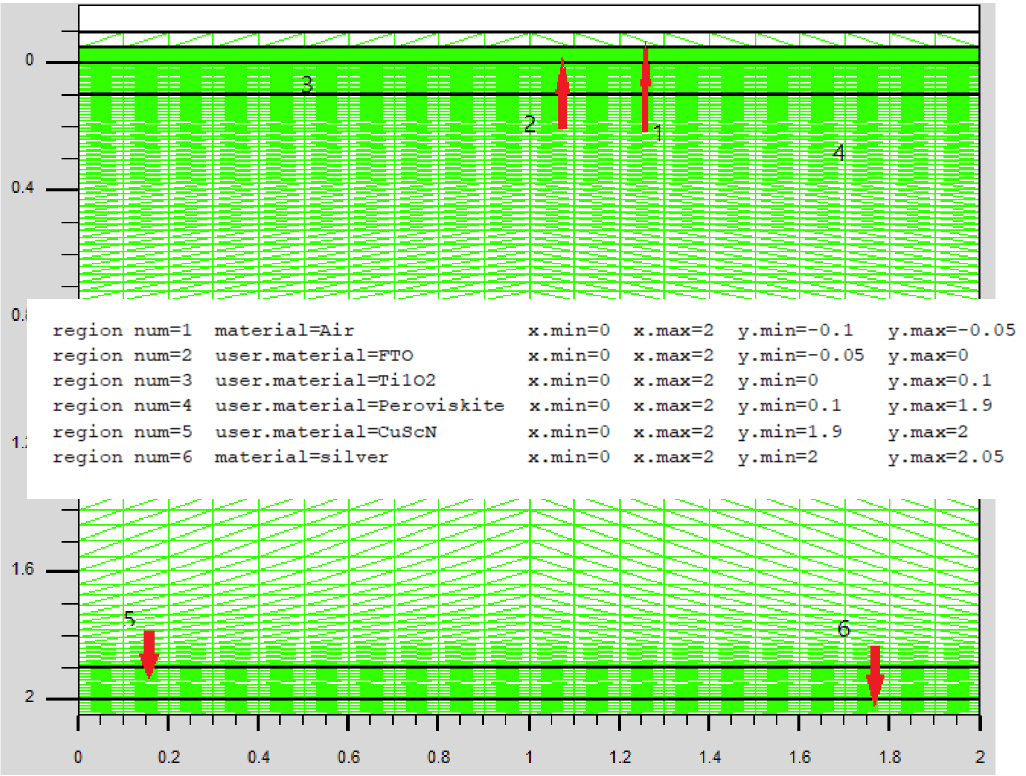

```
region num=1  material=Air                x.min=0  x.max=2  y.min=-0.1   y.max=-0.05
region num=2  user.material=FTO           x.min=0  x.max=2  y.min=-0.05  y.max=0
region num=3  user.material=Ti1O2         x.min=0  x.max=2  y.min=0      y.max=0.1
region num=4  user.material=Peroviskite   x.min=0  x.max=2  y.min=0.1    y.max=1.9
region num=5  user.material=CuScN         x.min=0  x.max=2  y.min=1.9    y.max=2
region num=6  material=silver             x.min=0  x.max=2  y.min=2      y.max=2.05
```

Figure III.2: Mesh in ATLAS for the studied solar cell.

REGION number=<integer> <material type>

<Position parameters>.

This statement can be broken up into several parts. First, the selected integer creates a region that can be referred to by that same integer. The material type determines what element or compound this region becomes and must be available in the ATLAS database. This can be selected out of Silvaco's own library or can be custom–made by the user. In addition, heterojunction grading between materials can also be described. Last, the position parameters tell ATLAS which potion of the mesh that was just created will become the region [127].

An example of created regions can be found in **Figure III.3**.

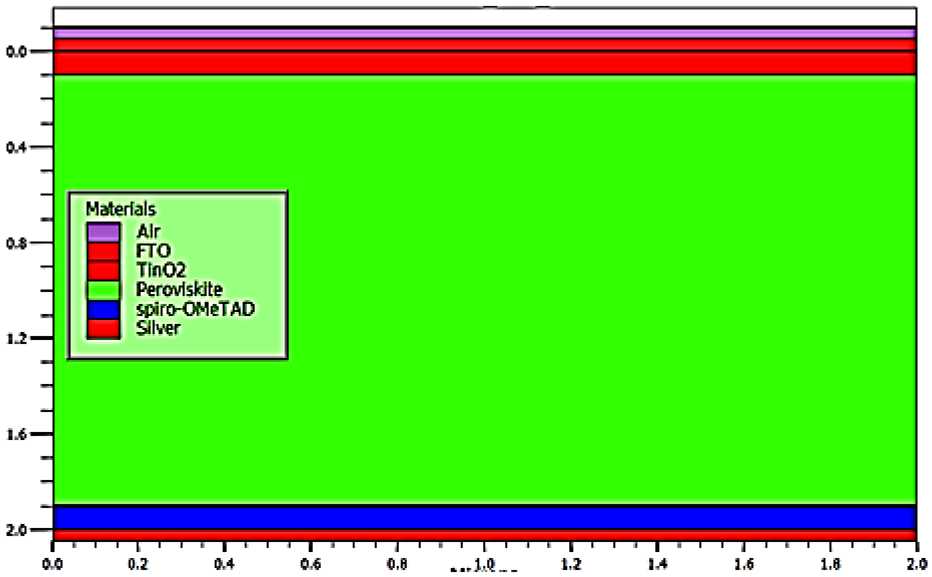

Figure III.3: Specified Regions.

III.3.3 Contacts

After defining the regions and materials, the next step is to create contacts on the device. To define the electrodes of the device, their position and size need to be entered. Additional information about their materials and work functions can be supplied if needed [127]. The format to define the electrodes is:

ELECTRODE NAME = <electrode name> <position>.

BOTTOM and TOP statements specify that the electrode be positioned along the bottom or the top of the device, respectively. Otherwise, minimum and maximum position boundaries must be specified, using the X.MIN, X.MAX, Y.MIN, Y.MAX statements [127].

An observation, in this work the only electrodes defined, are the anode and the cathode. However, Silvaco Atlas has a limit of 50 electrodes that can be defined [127].

III.3.4 Doping

After creating the separate regions and assigning materials to those regions, the materials themselves can be doped. The user specifies the doping using the DOPING statement:

DOPING <distribution type> <dopant type> <position parameters>.

The DOPING statement is broken down into three sections.

First, the distribution type can be either uniform, Gaussian, or complementary error function forms, only the uniform distribution type is utilized in this work. Next, a concentration and type of doping must be specified. Finally, the region to be doped must be identified [127].

III.3.5 Material

The previously defined and doped region must be associated with specific materials. Materials used throughout the simulation can be selected from a library that includes a number of common elements, compounds, and alloys. These have their most important parameters already defined. However, in solar cells, the use of exotic materials is not unusual. For such purposes, there is the ability to fully define already existing or brand new materials, down to their smallest detail. Such properties range from the essential bandgap and mobility all the way to light absorption coefficients. Contact information and work functions can also be entered here [127].

The general MATERIAL statement is:

MATERIAL <localization> <material definition>.

III.3.6 Models

More than seventy models can be used to achieve a better description of a full range of phenomena. Each model can be accompanied by a full set of its parameters when these differ from the default. Again, new models can be described using the C interpreter capability [127].

The physical models are grouped into five classes: mobility, recombination, carrier statistics, impact ionization, and tunneling. The list of physical models available to the ATLAS software can be found in the ATLAS user's manual [127]. The general MODELS statement is:

MODELS <model name>.

A specific example that specifies standard concentration dependent mobility, parallel field mobility, Shockley-Read-Hall recombination with fixed carrier lifetimes, and Fermi Dirac statistics is:

MODELS CONMOB FLDMOB SRH FERMIDIRAC.

III.3.7 Light Beam

When lighting is important for a device (like in solar cells), there is the ability to use a number of light sources and adjust their location, orientation, and intensity. The spectrum of the light can be described in all the necessary detail. Polarization, reflectivity, and ray trace are also among the simulator's features [127]. An optical beam is modeled as a collimated source using the BEAM statement of the form:

BEAM <parameters>.

The origin of the beam is defined by parameters X. ORIGIN and Y. ORIGIN, the ANGLE parameter specifies the direction of propagation of the beam relative to the x-axis, while ANGLE=90 describes a vertical illumination from the top of the device.

The beam is automatically split into a series of rays so that the sum of the rays covers the entire width of the illumination window. When the beam is split, ATLAS automatically resolves discontinuities along the region boundaries of the device. Rays are also split at interfaces between regions into a transmitted ray and a reflected ray [127].

For the purposes of this work, the source is the sun, and the **AM1.5** spectrum is used to simulate the energy received by a solar cell in a terrestrial application.

III.3.8 Solution Method

ATLAS contains several numerical methods to calculate the solutions to semiconductor device problems. There are three main types of numerical methods. The first method is the GUMMEL type, which is useful where the system of equations is weakly coupled but has only linear convergence. The next method is NEWTON, which is useful when the system of equations is strongly coupled and has quadratic convergence. This method causes ATLAS to spend extra time solving for quantities, which are essentially constant or weakly coupled and requires a more accurate initial guess to the problem to obtain convergence. The final method is the BLOCK method, which can provide faster simulation times in situations where the NEWTON method struggles. Numerical methods are given in the METHOD statements of the input file [127]. An example of an efficient METHOD statement is:

METHOD GUMMEL BLOCK NEWTON.

III.3.9 Solution Specification

This section of the input deck to ATLAS is where the simulation does its calculations to solve for the device specified. It is divided up into four parts: LOG, SOLVE, And LOAD

- **The LOG**

The statement creates a save file where all results of a run will be saved; Any DC, transient or AC data generated by “SOLVE” statements after the “LOG” statement will be saved [127]. An example LOG statement in which data is saved into example.log is:
LOG OUTFILE = example.log.

- **The SOLVE**

Solve statement follow the log statement and instructs Atlas to perform a solution for one or more specified bias points after getting an initial guess by solving the only Poisson equation, which means a simplified initial solution [127]. An example SOLVE statement that ramps the anode voltage from 0.0 V to 3.0 V with 0.01 V steps w is:
SOLVE VANODE=0.0 VSTEP=0.01 VFINAL=3.0 NAME=ANODE.

- **The LOAD and SAVE**

Statements are used together to help create better initial guesses for bias points. The SAVE statement is used first to store all of the information about the bias points, and later the LOAD statement is used to retrieve that information and aid in the solution [127]. The following are examples of the LOAD and SAVE instructions.

SAVE OUTF = SOL.STR

LOAD INFILE = SOL.STR.

III.3.10 Data Extraction and Plotting

The final section of the input deck is extracting the data and plotting it in a useful way. The two statements associated with this section are EXTRACT and TONYPLOT [127].

- **Extract**

The EXTRACT command allows extracting device parameters. It operates on the previous solved curve or structure file. By default, EXTRACT uses the currently open log file. To override this default, supply the name of a file to be used by EXTRACT before the extraction routine [127]. The EXTRACT statement is:
EXTRACT INIT INF="<filename>".

- **TonyPlot**

All graphics in Atlas is performed by saving a file and loading the file into TonyPlot. The TONYPLOT command causes Atlas to automatically save a structure file and plot it in TonyPlot. The TonyPlot window will appear displaying the material boundaries. Plot: Display menu is used to see more graphics options [127]. The TONYPLOT statement is:

TONYPLOT "<filename>".

III.4 Results and discussions

The perovskite solar cell (PSC) studied is shown in **Figure III.4**. It is similar to the first solid-state n-i-p PSC introduced by Kim et al. [28]. It consisted of methylammonium lead iodide ($MAPbI_3$) as a sensitizer, with a spiro-OMeTAD (2,2',7,7'-tetra-kis (N,N-di-p-methoxyphenylamine)-9,9'-spirobifluorene) as an HTM and TiO2 as an ETM. The band gap energy diagram simulated by Atlas at equilibrium is presented is **Figure III.5**. A suitable alignment is achieved with a good selectivity of electrons toward the ETL and holes towards the HTL.

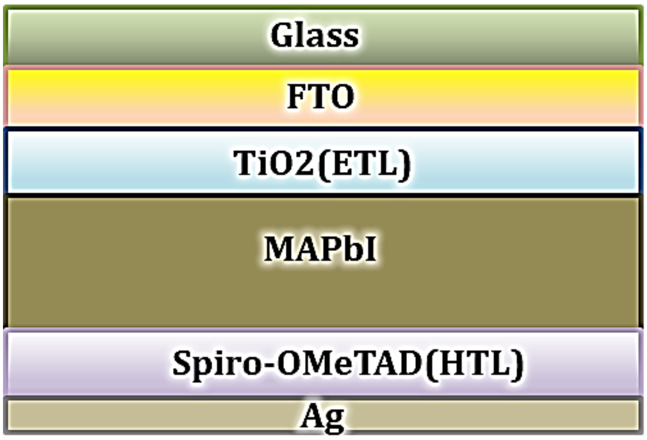

Figure III.4: Preliminary device structure.

The physical input parameters used in the simulation are summarized in **Table III.1**.

Table III.1: Physical parameters used in the simulation [128].

Paramater	**Designation**	**FTO**	**TiO_2**	**$MAPbI_3$**	**Spiro-OMeTAD**
E_g (eV)	**Gap energy**	3.5	3.2	1.55	3.3
$q\chi_s\ (eV)$	**Affinity**	4.2	4.1	3.9	2.45
N_c (cm^{-3})	**Effective density of Conduction band (× 10^{19})**	0.22	20	1	1
N_v (cm^{-3})	**Effective density of Conduction band (× 10^{19})**	0.02	10	0.1	1
$\mu_n(cm^2V^{-1}s^{-1})$	**Electron mobility**	300	20	40	10^{-3}
$\mu_p(cm^2V^{-1}s^{-1})$	**Hole mobility**	10	10	10	10^{-4}
ε_r	**Relative dielectric constant**	9	9	10.7	9

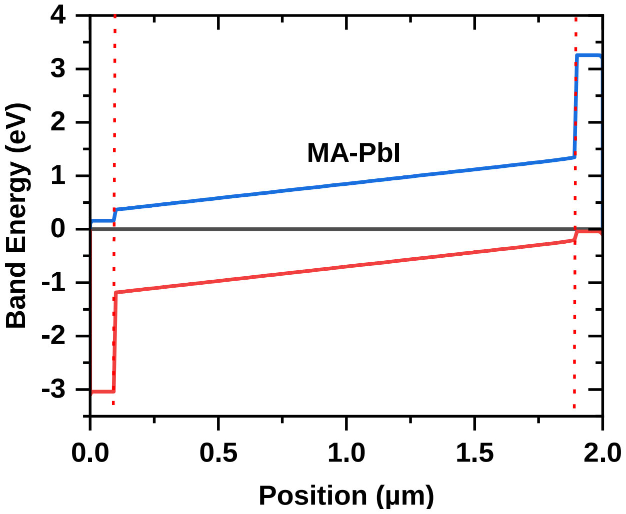

Figure III.5: Band gap energy diagram at equilibrium.

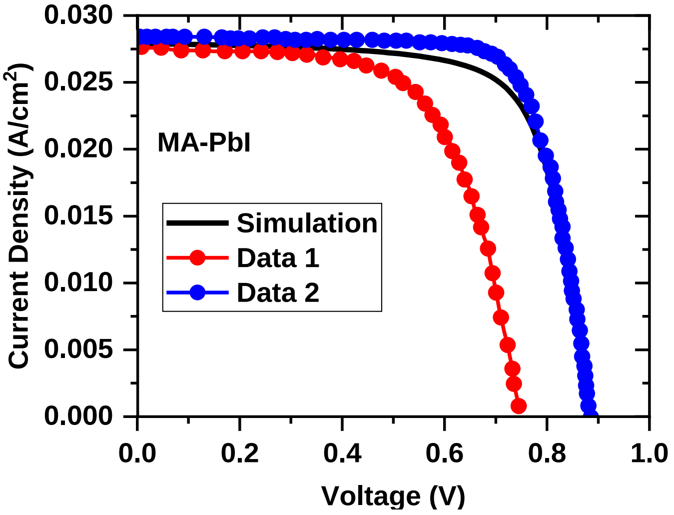

Figure III.6: J-V characteristic, simulation and experimental data 1 from [1] and data 2 from [129].

Table III.2: Electrical outputs for the preliminary device structure.

	$J_{sc}(mA/cm^2)$	$V_{oc}(V)$	FF	$PCE\%$
Simulation	27.91	0.88	0.72	17.71
Data 1 [1]	27.65	0.75	0.63	13.20
Data 2 [129]	28.24	0.88	0.76	18.94

The J-V characteristic is presented in **Figure III.6** and compared with experimental data from [1,129]. The simulated result is comparable to the experimental range and a good photo-conversion efficiency (*PCE*) of 17.71% is obtained. The external quantum efficiency (EQE) shown in **Figure III. 7** exhibits a good spread over the range UV-Visible-Infrared.

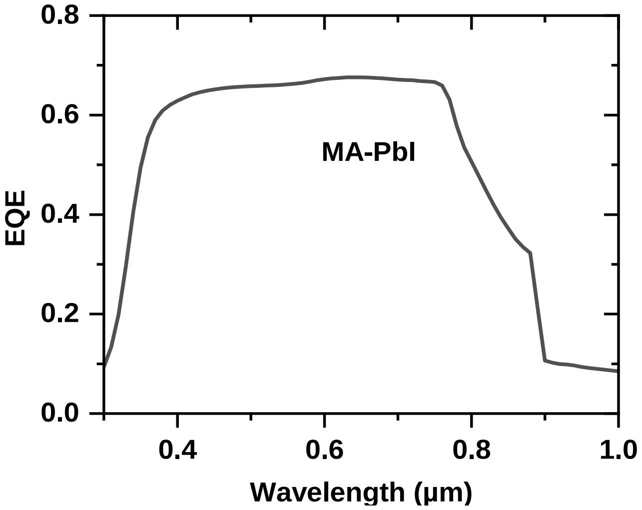

Figure III.7: EQE of the preliminary device structure.

III.4.1 The use of CuScN as HTM

Hole transport materials play different crucial roles, such as: (i) blocking electron transfer to the back-contact metal electrode, (ii) extraction of photo-generated holes from the perovskite and transportation of these extracted charges back to the back-contact metal electrode, and (iii) prevent direct contact between the metal electrode and the perovskite layer [130]. An ideal HTM should exhibit properties, such as: (i) high hole mobility, chemical stability and thermal robustness to with stand annealing process during fabrication of the PSC; (ii) the highest occupied molecular orbital (HOMO) energy level should match the valence band energy of the perovskite; (iii) should protect the perovskite layer from air and moisture and be able to prevent the diffusion of external moieties or elements inside the photo-absorber. Moreover, the HTM should have a low annealing temperature and short annealing times to avoid degradation of the underlying layers. Last but not least, the HTM (iv) should show minimum absorption in the visible and near-infrared of the solar spectrum to avoid absorption of photons during the photo-excitation of excitons [130].

Even though the use of spiro-OMeTAD led to improved performance of PSC, spiro-OMeTAD suffers from low hole mobility of about $6 \times 10^{-5} cm^2 V^{-1} s^{-1}$, and used commonly with additives that induced the degradation of the perovskite layer, thus leading to long-term PSCs instability. Moreover, it present several limitations as it is costly to manufacture and the synthesis routes are tedious which does not augur well for large-scale fabrication, thus making it not viable for commercial production [130]. Therefore, research efforts were centered at finding affordable HTMs with improved hole mobility, stability, and a feasible synthesis route [130].

Consequently inorganic HTMs such as CuI, CuSCN, NiO, and Cu2O have potentially better stability than organic HTMs and have been also tested in PSCs [130]. One such promising inorganic HTM is CuSCN, which is an inexpensive and abundant metal pseudo-halide of singly ionized copper. It has a well-aligned work function and has demonstrated high mobility as well as good thermal stability [130]. Therefore in this section the organic HTM is replaced by inorganic CuScN, HTM.

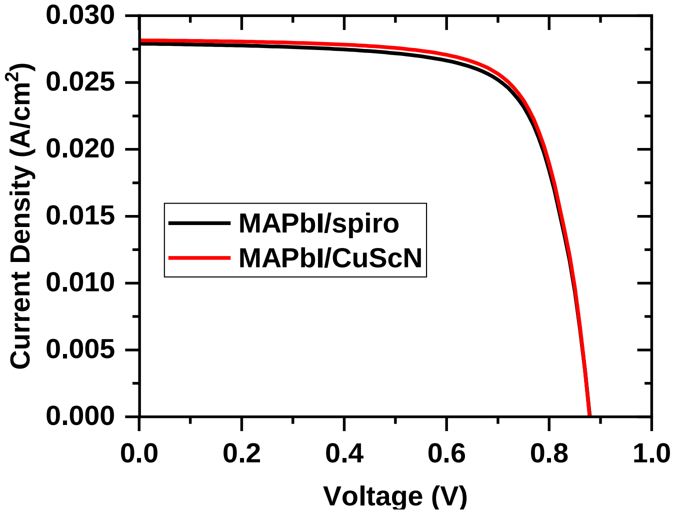

Figure III.8 - J-V characteristic when the organic HTM is replaced by inorganic CuScN.

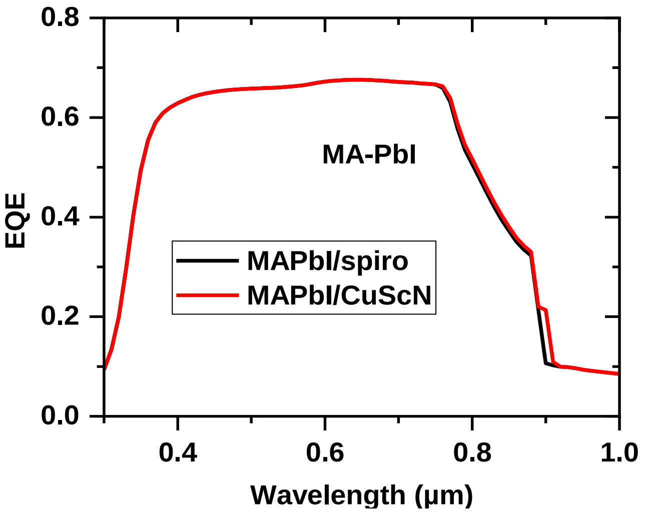

Figure III.9: EQE when the organic HTM is replaced by inorganic CuScN.

Table III.3: Electrical outputs when the organic HTM is replaced by inorganic CuScN.

HTM	$J_{sc}(mA/cm^2)$	$V_{oc}(V)$	FF	$PCE\%$
Spiro-OMeTED	27.91	0.88	0.72	17.71
CuScN	28.15	0.88	0.73	18.03

According the obtained results a slight improvement is noticed in J_{SC}, in the *PCE* of the cell which increases from 17.71% to 18.03% and also in the EQE **(Figure III.9)**.

III.4.2 Effect of replacing a fraction of Pb by Sn

Replacing Pb (which is toxic) by Sn induces a reduction in the band gap energy of the perovskite material lower than 1.55 eV (see **chapter II.4.1**). Therefore it is desirable to enlarge first the band gap of the perovskite, then replacing Pb by Sn. The increase of the band gap can be achieved by replacing the I_3 by Cl_3. Then it increases from 1.55 eV of the $MAPbI_3$ to 2.92 eV of the $MAPbCl_3$ [131]. The band gap diagram in this case is presented in **Figure III.10** and the

HTM used is CuScN. The extinction index from which the absorbance is calculated is presented in **Figure III.11** for all perovskite varieties used in the study. As we can see a shift toward shorter wavelength is noticed when the band gap energy is extended.

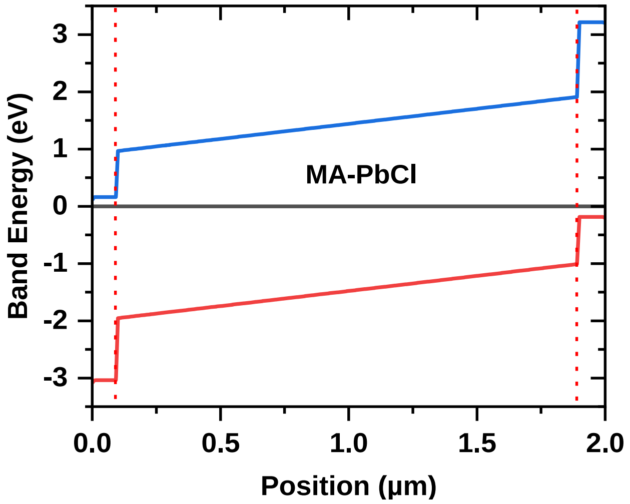

Figure III.10: Band gap energy diagram at equilibrium for MAPbCl perovskite.

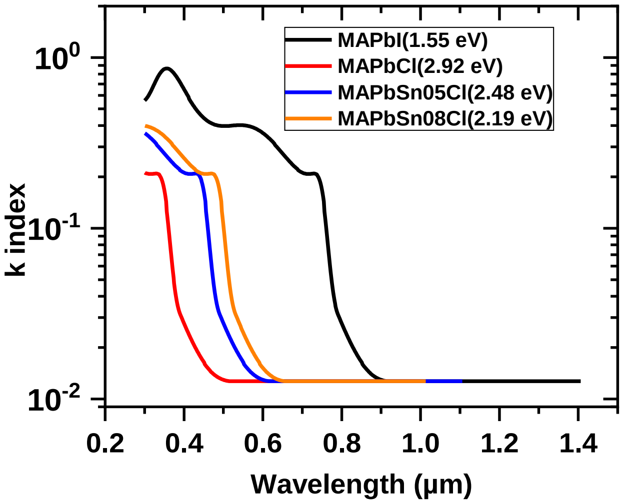

Figure III.11: Extinction optical index for the different studied perovskites when a fraction of Pb is replaced by Sn [131].

It is obvious that the increase of the band gap energy over 2 eV causes a serious reduction in J_{SC} (**Figure III.12**) and EQE (**Figure III.13**) since additional losses in photon absorption occurred, while *Voc* increases.

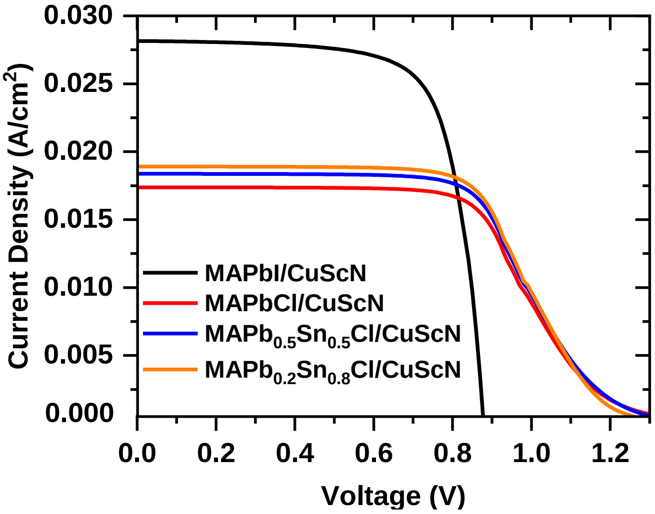

Figure III.12: J-V characteristics simulated for the different perovskite materials when a fraction of Pb is replaced by Sn.

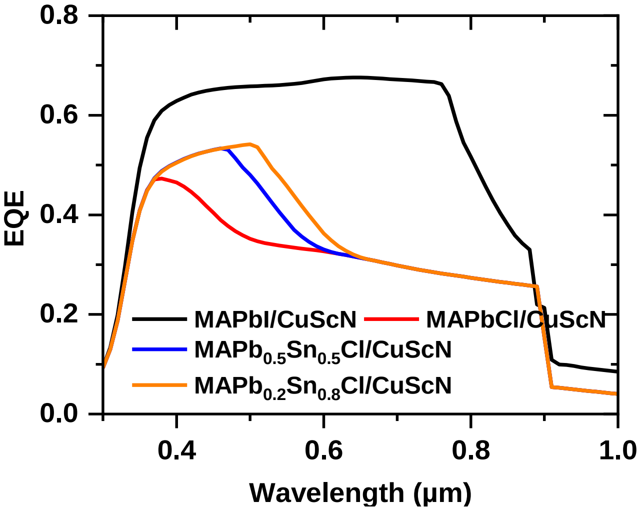

Figure III.13: EQE simulated for the different perovskite materials when a fraction of Pb is replaced by Sn.

With MAPbCl the band gap energy reached 2.92 eV, J_{SC} decreases to 17.38 mA/cm^2 while V_{OC} increases to 1.3 V. The obtained *PCE* in this case is 13.63% with an important diminution in *FF* to 0.6. When the fraction of Sn reaches 80% the band gap energy decreases to 2.19 eV and the obtained PCE in this case is 14.79% . This efficiency is acceptable by regarding the benefit of reducing Pb in the perovskite material.

Table III.4: Electrical outputs for the different perovskite materials when a fraction of Pb is replaced by Sn

Perovskite	$J_{sc}(mA/cm^2)$	$V_{oc}(V)$	FF	$PCE\%$
MAPbI	28.15	0.88	0.73	18.03
MAPbCl	17.38	1.30	0.603	13.63
$MAPb_{0.5}Sn_{0.5}Cl$	18.37	1.29	0.607	14.38
$MAPb_{0.2}Sn_{0.8}Cl$	18.91	1.24	0.630	14.79

III.4.3 Comparison with experimental data

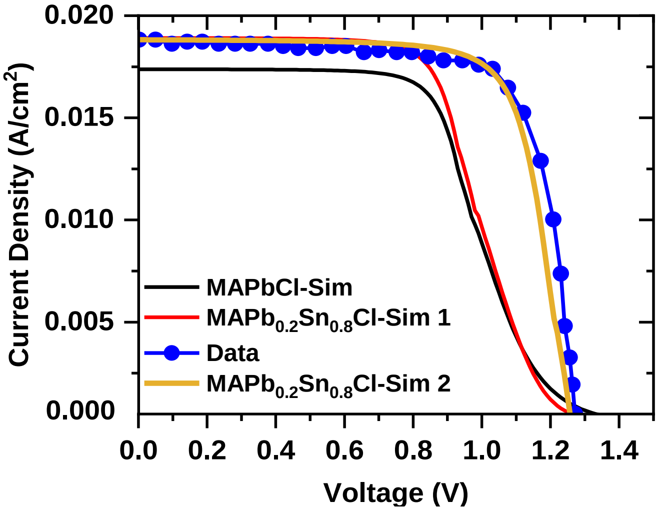

Figure III.14: J-V characteristics simulated and compared to data [132].

In **Figure III.14** we compare the obtained simulation results with experimental data [132]. As we can see, a noticeable difference is observed mainly in FF and PCE. Consequently, a second simulation procedure was performed in the aim to obtain better fitting with data. This is done by trying to reduce carefully V_{OC} so that the FF increases until the wanted fitting is achieved. We suggest the formation of interlayers between both the ETL, HTL and the perovskite material. These interlayers are justified since the surface of the perovskite can react easily with ETM(HTM) [1]. We propose that interlayers have intermediate properties between that of ETM(HTM) and the perovskite and are presented in the band gap energy diagram at equilibrium in **Figure III.15**.

Fortunately, the best fitting with experiments was indeed achieved by considering simulation procedure 2 as shown in **Figure III.14**. The extracted electrical outputs are summarised in **Table III.5**. Good agreement between the simulated and experimental electrical outputs is obtained with a simulated PCE of 17.76% inferior slightly to the experimental one (17.95%).

Table III.5: Electrical outputs simulated and compared to experimental data from [132].

Perovskite	$J_{sc}(mA/cm^2)$	$V_{oc}(V)$	FF	$PCE\%$
MAPbCl	17.38	1.30	0.603	13.63
$MAPb_{0.2}Sn_{0.8}Cl$ (Sim 1)	18.91	1.24	0.630	14.79
$MAPb_{0.2}Sn_{0.8}Cl$ (Sim 2)	18.82	1.26	0.749	17.76
Data [132]	18.82	1.27	0.751	17.95

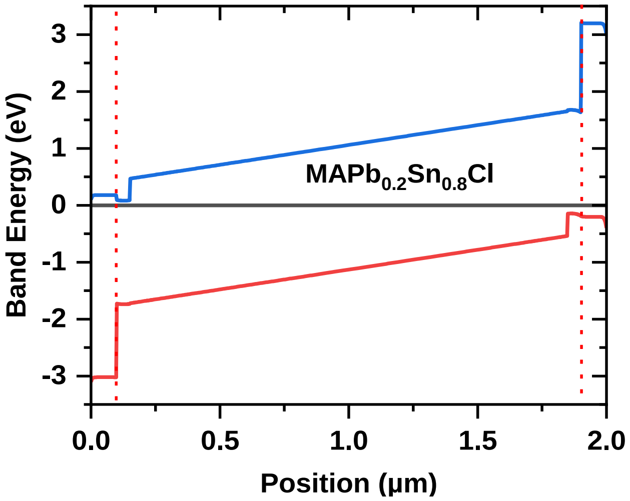

Figure III.15: Band gap energy diagram at equilibrium for $MAPb_{0.2}Sn_{0.8}Cl_3$ perovskite with interlayers between ETL(HTL) and the perovskite.

III.5 Optimization

In this section, the reduction of the Pb amount will be extended to $MAPbI_3$ (1.55 eV) and the resulting perovskite will be used as the absorbent material of rear (bottom) n-i-p solar cell. When 50% of Pb is replaced by 50% of Sn, the band gap energy is lowered to 1.18 eV [129]. Consequently longer wavelength photons will be absorbed by the bottom solar cell. An schematic diagram of the tandem solar cell ($MAPb_{0.2}Sn_{0.8}Cl$(2.19eV)/$MAPb_{0.5}Sn_{0.5}I$(1.18eV)) is illustrated in **Figure III.16**.

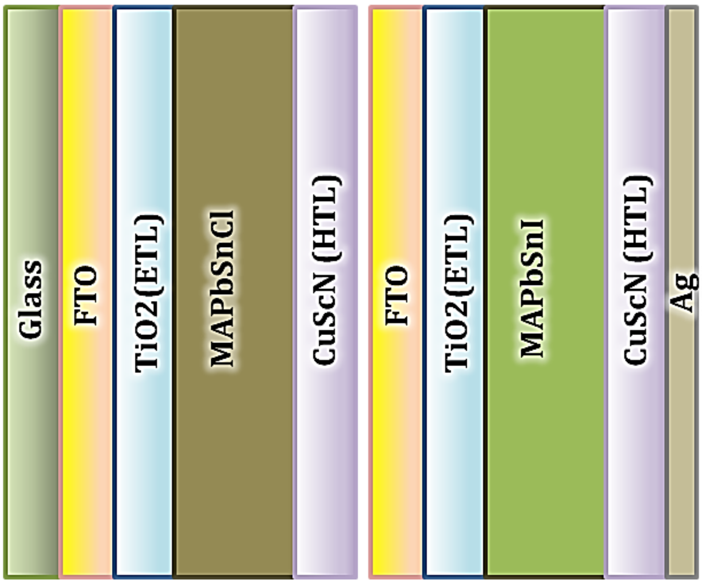

Figure III.16: The suggested structure of the tandem solar cell.

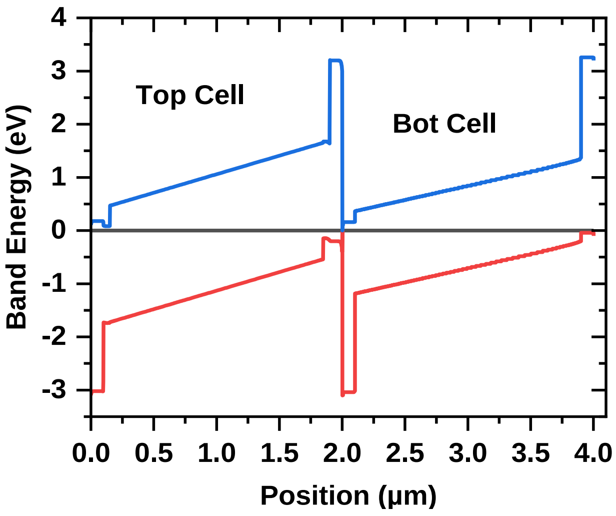

Figure III.17: Band gap diagram at equilibrium of the Tandem solar cell.

The band gap diagram at the equilibrium is shown in **Figure III.17**. We notice that the passage of photo-generated carriers through the interface region between the top and the bottom cell is supposed to occur perfectly by tunneling. This, since the HTL of the top cell and the ETL of the bottom one are thins enough with a good alignment between the allowed band states.

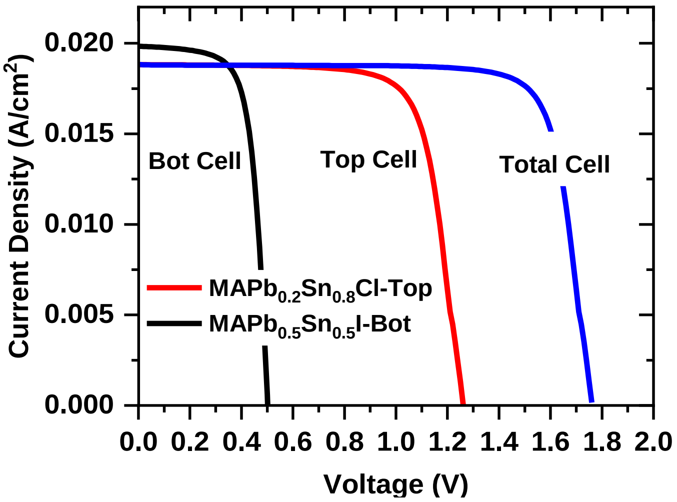

Figure III.18: J-V characteristic of the top, bottom and the tandem cell.

Table III.6: Simulated electrical outputs of the top, bottom and the tandem (total) solar cell.

Cell	$J_{sc}(mA/cm^2)$	$V_{oc}(V)$	FF	$PCE\%$
Top Cell	18.82	1.26	0.749	17.76
Bottom Cell	19.84	0.5	0.697	6.92
Tandem cell	18.82	1.75	0.804	26.48

The obtained J-V characteristics are illustrated in **Figure III.18** and the extracted outputs are summarized in **Table III.6**. Since the top and the bottom cell are serial connected the lower J_{SC} is dominant over the tandem cell while V_{OC} is almost the sum of the two cells. Consequently, in this perfect case when the tunnelling is ideal and any losses by recombination between top and bottom cells are omitted, the PCE can reach a remarkable value of 26.48% with a good FF of 0.804. It was not able for us to acquire experimental data for comparison, since the effect of reducing Pb amount by replacing it by Sn was tested only in single junction of the perovskite solar cell. For the last one, in addition many type of perovskite was studied with different composition and different ETM (HTM). Therefore, it was very difficult to acquire pertinent data even for the single junction solar cell. Nevertheless, the study of this tandem cell can give initial interest on the crucial role of reducing Pb by Sn and since this has an effect on band gap energy why not to exploiting it in tandem solar cell's technology.

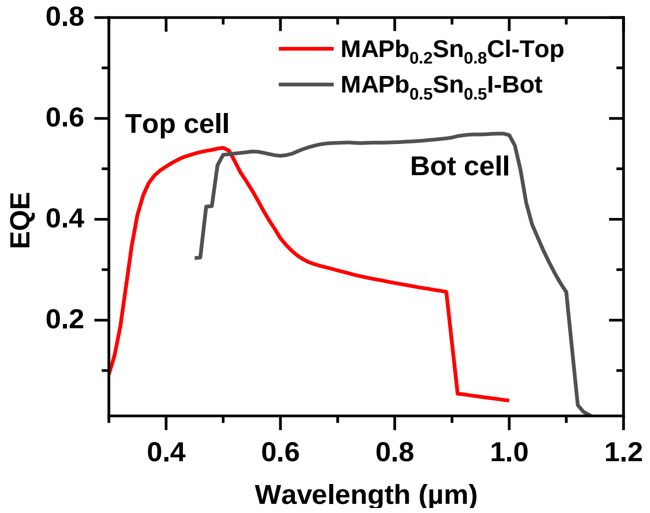

Figure III.19: EQE of the top, bottom and the tandem cell.

From **Figure III.19** which shows the EQE of the top and the bottom solar cell, we can see how the total EQE was extended to longer wavelengths (~1.2 µm).

III.6 Conclusion

We have studied by numerical simulation using Silvaco-Atlas a perovskite based n-i-p solar cell. The preliminary device structure was FTO/TiO_2(ETL)/$MAPbI_3$(Perovskite)/Spiro-OMeTAD(HTL)/ Ag. The obtained electrical outputs was in the experimental range ($J_{sc} = 27.91 \frac{mA}{cm^2}$; $V_{oc} = 0.88\,V; FF = 0.72; PCE = 17.71\%$). The main aim of this study is to reduce the amount of the toxic Pb by replacing it with Sn and preserving a useful PCE of the solar cell. This was done first by increasing the band gap energy of the perovskite by changing I by Cl and changing the organic HTM by inorganic one (CuScN). The band gap of the perovskite reached to 2.92 eV. Then, the Pb amount was reduced to 20% while the Sn was increased to 80%. The band gap decreases to 2.19 eV and the obtained outputs in agreement with experimental range was $J_{SC} = 18.82 \frac{mA}{cm^2}$; $V_{OC} = 1.26\,V; FF = 0.749; PCE = 17.76\%$. The use of Sn was extended to MAPbI and the amount of Pb was reduced by 50%. The resulting perovskite was used as the absorbent region of a second n-i-p bottom cell of a tandem structure while the previous cell was used as the top cell. Under these considerations the predictable electrical outputs found was $J_{sc} = 18.82 \frac{mA}{cm^2}$; $V_{oc} = 1.75\,V; FF = 0.804; PCE = 26.48\%$, when a perfect tunnelling is considered (without losses by recombination) through the interlayer between the top and the bottom cells.

Final Conclusion

Final Conclusion

Hybrid halide perovskites have attracted great attention in photovoltaic solar cell's technology. However they suffer from two main problems: a rather poor stability and high toxicity due to Pb in the perovskite material. The aim of this master dissertation is the study of the possibility of replacing partially Pb by Sn in two different perovskite materials; $MAPbCl_3$ and $MAPbI_3$. The solar cell structure is the standard n-i-p. The top contact is FTO, the n layer is TiO_2 (named ETL) and the bottom contact is Ag (silver). However for the p layer two materials are suggested: organic Spiro-OMeTAD and inorganic CuScN.

The study is based on numerical simulation by Silvaco-Atlas, which is a powerful software for 2D, and 3D electronic device's modelling. The simulated results are also compared with available measurement to certify the study. The studied PSC at the first is FTO/TiO_2/MAPbI/ spiro-OMeTAD (n-i-p) that gave electrical outputs similar to experimental range; $J_{SC} = 27.91 \frac{mA}{cm^2}, V_{OC} = 0.88\ V, FF = 0.72\ , PCE = 17.71\%$.

After that and since the organic HTM (spiro-OMeTAD), according to many works, suffered from instability, we have replaced it by the inorganic HTM CuScN and as results a slight further improvement was occurred in $J_{sc} = 28.15 \frac{mA}{cm^2}$. Next we have concentrated on the main goal of the work with is replacing partially Pb by Sn by considering the $MAPbCl_3$ perovskite which has band gap of 2.92 eV. With 80% of Sn and 20% of Pb the band gap is reduced to 2.19 eV and the solar cell gave good electrical outputs similar to experimental data; $J_{SC} = 18.82 \frac{mA}{cm^2}, V_{OC} = 1.26\ V, FF = 0.749\ , PCE = 17.76\%$.

The band gap reduction that occurs with the partial replacement of Pb with Sn is used in the design of a Tandem solar cell where the perovskite material of the top cell is $MAPb_{0.2}Sn_{0.8}Cl_3$ (2.19 eV) while that of the bottom one is $MAPb_{0.5}Sn_{0.5}I_3$ (1.18 eV). By considering the ideal performance of the cell a very interesting outputs was obtained; $J_{SC} = 18.82 \frac{mA}{cm^2}, V_{OC} = 1.75\ V, FF = 0.804\ , PCE = 26.48\%$.

As perspective, we visualize to enlarge the study taking into account the probable defects in the single n-i-p structure and the non-perfect tunneling between the top and bottom cell in the tandem structure.

References

[1] Gollino L and Pauporté T 2021 Lead-Less Halide Perovskite Solar Cells *Sol. RRL* **5** 2000616

[2] Leyden M R, Terakawa S, Matsushima T, Ruan S, Goushi K, Auffray M, Sandanayaka A S D, Qin C, Bencheikh F and Adachi C 2019 Distributed Feedback Lasers and Light-Emitting Diodes Using 1-Naphthylmethylamnonium Low-Dimensional Perovskite *ACS Photonics* **6** 460–6

[3] Wei Y, Cheng Z and Lin J 2019 An overview on enhancing the stability of lead halide perovskite quantum dots and their applications in phosphor-converted LEDs *Chem. Soc. Rev.* **48** 310–50

[4] Pallares R M, Su X, Lim S H and Thanh N T K 2016 Fine-tuning of gold nanorod dimensions and plasmonic properties using the Hofmeister effects *J. Mater. Chem. C* **4** 53–61

[5] Mykhaylyk V B, Kraus H and Saliba M 2019 Bright and fast scintillation of organolead perovskite $MAPbBr_3$ at low temperatures *Mater. Horiz.* **6** 1740–7

[6] Zhang J, Barboux P and Pauporté T 2014 Electrochemical Design of Nanostructured ZnO Charge Carrier Layers for Efficient Solid-State Perovskite-Sensitized Solar Cells *Adv. Energy Mater.* **4** 1400932

[7] Kojima A, Teshima K, Shirai Y and Miyasaka T 2009 Organometal Halide Perovskites as Visible-Light Sensitizers for Photovoltaic Cells *J. Am. Chem. Soc.* **131** 6050–1

[8] Chung I, Lee B, He J, Chang R P H and Kanatzidis M G 2012 All-solid-state dye-sensitized solar cells with high efficiency *Nature* **485** 486–9

[9] Yin W-J, Shi T and Yan Y 2014 Unique Properties of Halide Perovskites as Possible Origins of the Superior Solar Cell Performance *Adv. Mater.* **26** 4653–8

[10] Stoumpos C C, Malliakas C D and Kanatzidis M G 2013 Semiconducting Tin and Lead Iodide Perovskites with Organic Cations: Phase Transitions, High Mobilities, and Near-Infrared Photoluminescent Properties *Inorg. Chem.* **52** 9019–38

[11] Stranks S D, Eperon G E, Grancini G, Menelaou C, Alcocer M J P, Leijtens T, Herz L M, Petrozza A and Snaith H J 2013 Electron-Hole Diffusion Lengths Exceeding 1 Micrometer in an Organometal Trihalide Perovskite Absorber *Science* **342** 341–4

[12] Sutton R J, Eperon G E, Miranda L, Parrott E S, Kamino B A, Patel J B, Hörantner M T, Johnston M B, Haghighirad A A, Moore D T and Snaith H J 2016 Bandgap-Tunable Cesium Lead Halide Perovskites with High Thermal Stability for Efficient Solar Cells *Adv. Energy Mater.* **6** 1502458

[13] Anon Best Research-Cell Efficiency Chart

[14] Wang Y, Zhang T, Kan M and Zhao Y 2018 Bifunctional Stabilization of All-Inorganic α-$CsPbI_3$ Perovskite for 17% Efficiency Photovoltaics *J. Am. Chem. Soc.* **140** 12345–8

[15] Saliba M, Matsui T, Domanski K, Seo J-Y, Ummadisingu A, Zakeeruddin S M, Correa-Baena J-P, Tress W R, Abate A, Hagfeldt A and Grätzel M 2016 Incorporation of rubidium cations into perovskite solar cells improves photovoltaic performance *Science* **354** 206–9

[16] Toscano C D and Guilarte T R 2005 Lead neurotoxicity: From exposure to molecular effects *Brain Res. Rev.* **49** 529–54

[17] Abate A 2017 Perovskite Solar Cells Go Lead Free *Joule* **1** 887

[18] Scaife E Crystal Preparation and Properties of Cesium Tin(U) Trihalides 7

[19] Jones N L, Harlow R L, Herron N, Thorn D L and Wang Y Preparation and Characterization of Layered Lead Halide Compoundst 3

[20] E B M 1839 Memoire sur les Effets Electriques Produits sous l’Influence des Rayons Solaires *Comptes Rendus Hebd. Seances Acad. Sci.* **9** 561–7

[21] Anon Champion Photovoltaic Module Efficiency Chart

[22] Green M A, Dunlop E D, Hohl-Ebinger J, Yoshita M, Kopidakis N and Hao X 2020 Solar cell efficiency tables (version 56) *Prog. Photovolt. Res. Appl.* **28** 629–38

[23] Parsons I 2004 H.-R. Wenk and A. Bulakh, Minerals: Their Constitution and Origin. Cambridge University Press, 2004, xxii + 646 pp. Price £95 (US 70) (paperback) ISBN 0 52152958 1. *Mineral. Mag.* **68** 720–4

[24] Wells H L 1893 Über die Cäsium- und Kalium-Bleihalogenide *Z. Für Anorg. Chem.* **3** 195–210

[25] Weber D 1978 $CH_3NH_3PbX_3$, ein Pb(II)-System mit kubischer Perowskitstruktur / $CH_3NH_3PbX_3$, a Pb(II)-System with Cubic Perovskite Structure *Z. Für Naturforschung B* **33** 1443–5

[26] Mitzi D B, Wang S, Feild C A, Chess C A and Guloy A M 1995 Conducting Layered Organic-Inorganic Halides Containing -Oriented Perovskite Sheets *Sci. New Ser.* **267** 1473–6

[27] Im J-H, Lee C-R, Lee J-W, Park S-W and Park N-G 2011 6.5% efficient perovskite quantum-dot-sensitized solar cell *Nanoscale* **3** 4088–93

[28] Kim H-S, Lee C-R, Im J-H, Lee K-B, Moehl T, Marchioro A, Moon S-J, Humphry-Baker R, Yum J-H, Moser J E, Grätzel M and Park N-G 2012 Lead Iodide Perovskite Sensitized All-Solid-State Submicron Thin Film Mesoscopic Solar Cell with Efficiency Exceeding 9% *Sci. Rep.* **2** 591

[29] Oku T 2020 Crystal structures of perovskite halide compounds used for solar cells *Rev. Adv. Mater. Sci.* **59** 264–305

[30] Tilley R J D 2016 *Perovskites: Structure-Property Relationships* (John Wiley & Sons)

[31] Green M A, Ho-Baillie A and Snaith H J 2014 The emergence of perovskite solar cells *Nat. Photonics* **8** 506–14

[32] Domanski K The Quest for Stability of Perovskite Solar Cells: Understanding Degradation, Improving Lifetimes and Towards Experimental Standards 218

[33] Christians J A, Fung R C M and Kamat P V 2014 An Inorganic Hole Conductor for Organo-Lead Halide Perovskite Solar Cells. Improved Hole Conductivity with Copper Iodide *J. Am. Chem. Soc.* **136** 758–64

[34] Park N-G 2015 Perovskite solar cells: an emerging photovoltaic technology *Mater. Today* **18** 65–72

[35] Olthof S 2016 Research Update: The electronic structure of hybrid perovskite layers and their energetic alignment in devices *APL Mater.* **4** 091502

[36] Watthage S C, Song Z, Phillips A B and Heben M J 2018 Chapter 3 - Evolution of Perovskite Solar Cells *Perovskite Photovoltaics* ed S Thomas and A Thankappan (Academic Press) pp 43–88

[37] Miyasaka T 2018 Lead Halide Perovskites in Thin Film Photovoltaics: Background and Perspectives *Bull. Chem. Soc. Jpn.* **91** 1058–68

[38] Umebayashi T, Asai K, Kondo T and Nakao A 2003 Electronic structures of lead iodide based low-dimensional crystals *Phys. Rev. B* **67** 155405

[39] Brivio F, Butler K T, Walsh A and van Schilfgaarde M 2014 Relativistic quasiparticle self-consistent electronic structure of hybrid halide perovskite photovoltaic absorbers *Phys. Rev. B* **89** 155204

[40] Li Z, Kulkarni S A, Boix P P, Shi E, Cao A, Fu K, Batabyal S K, Zhang J, Xiong Q, Wong L H, Mathews N and Mhaisalkar S G 2014 Laminated Carbon Nanotube Networks for Metal Electrode-Free Efficient Perovskite Solar Cells *ACS Nano* **8** 6797–804

[41] Li Z, Klein T R, Kim D H, Yang M, Berry J J, van Hest M F A M and Zhu K 2018 Scalable fabrication of perovskite solar cells *Nat. Rev. Mater.* **3** 18017

[42] Yilbas B S, Al-Sharafi A and Ali H 2019 Surfaces for Self-Cleaning *Self-Cleaning of Surfaces and Water Droplet Mobility* (Elsevier) pp 45–98

[43] Yang M, Li Z, Reese M O, Reid O G, Kim D H, Siol S, Klein T R, Yan Y, Berry J J, van Hest M F A M and Zhu K 2017 Perovskite ink with wide processing window for scalable high-efficiency solar cells *Nat. Energy* **2** 17038

[44] Tang S, Deng Y, Zheng X, Bai Y, Fang Y, Dong Q, Wei H and Huang J 2017 Composition Engineering in Doctor-Blading of Perovskite Solar Cells *Adv. Energy Mater.* **7** 1700302

[45] Ding X, Liu J and Harris T A L 2016 A review of the operating limits in slot die coating processes *AIChE J.* **62** 2508–24

[46] Chang W-C, Lan D-H, Lee K-M, Wang X-F and Liu C-L 2017 Inside Cover: Controlled Deposition and Performance Optimization of Perovskite Solar Cells Using Ultrasonic Spray-Coating of Photoactive Layers (ChemSusChem 7/2017) *ChemSusChem* **10** 1301–1301

[47] Das S, Yang B, Gu G, Joshi P C, Ivanov I N, Rouleau C M, Aytug T, Geohegan D B and Xiao K 2015 High-Performance Flexible Perovskite Solar Cells by Using a Combination of Ultrasonic Spray-Coating and Low Thermal Budget Photonic Curing *ACS Photonics* **2** 680–6

[48] Liang Z, Zhang S, Xu X, Wang N, Wang J, Wang X, Bi Z, Xu G, Yuan N and Ding J 2015 A large grain size perovskite thin film with a dense structure for planar heterojunction solar cells via spray deposition under ambient conditions *RSC Adv.* **5** 60562–9

[49] Heo J H, Lee M H, Jang M H and Im S H 2016 Highly efficient $CH_3NH_3PbI_{3-x}Cl_x$ mixed halide perovskite solar cells prepared by re-dissolution and crystal grain growth via spray coating *J. Mater. Chem. A* **4** 17636–42

[50] Mohamad D K, Griffin J, Bracher C, Barrows A T and Lidzey D G 2016 Spray-Cast Multilayer Organometal Perovskite Solar Cells Fabricated in Air *Adv. Energy Mater.* **6** 1600994

[51] Hong S C, Lee G, Ha K, Yoon J, Ahn N, Cho W, Park M and Choi M 2017 Precise Morphology Control and Continuous Fabrication of Perovskite Solar Cells Using Droplet-Controllable Electrospray Coating System *ACS Appl. Mater. Interfaces* **9** 7879–84

[52] Li S-G, Jiang K-J, Su M-J, Cui X-P, Huang J-H, Zhang Q-Q, Zhou X-Q, Yang L-M and Song Y-L 2015 Inkjet printing of $CH_3NH_3PbI_3$ on a mesoscopic TiO_2 film for highly efficient perovskite solar cells *J. Mater. Chem. A* **3** 9092–7

[53] Shi Z and Jayatissa A 2018 Perovskites-Based Solar Cells: A Review of Recent Progress, Materials and Processing Methods *Materials* **11** 729

[54] SALA G *Hybrid perovskite-based solar cells: photoactive layer morphology optimization towards printed devices.* (Politecnico di Milano)

[55] Ko H-S, Lee J-W and Park N-G 2015 15.76% efficiency perovskite solar cells prepared under high relative humidity: importance of PbI2 morphology in two-step deposition of CH3NH3PbI3 *J. Mater. Chem. A* **3** 8808–15

[56] Song Z, Watthage S C, Phillips A B and Heben M J 2016 Pathways toward high-performance perovskite solar cells: review of recent advances in organo-metal halide perovskites for photovoltaic applications *J. Photonics Energy* **6** 022001

[57] Liu M, Johnston M B and Snaith H J 2013 Efficient planar heterojunction perovskite solar cells by vapour deposition *Nature* **501** 395–8

[58] Zhou H, Chen Q, Li G, Luo S, Song T, Duan H-S, Hong Z, You J, Liu Y and Yang Y 2014 Interface engineering of highly efficient perovskite solar cells *Science* **345** 542–6

[59] Boix P P, Nonomura K, Mathews N and Mhaisalkar S G 2014 Current progress and future perspectives for organic/inorganic perovskite solar cells *Mater. Today* **17** 16–23

[60] Jeon N J, Noh J H, Yang W S, Kim Y C, Ryu S, Seo J and Seok S I 2015 Compositional engineering of perovskite materials for high-performance solar cells *Nature* **517** 476–80

[61] Lee J-W, Seol D-J, Cho A-N and Park N-G 2014 High-Efficiency Perovskite Solar Cells Based on the Black Polymorph of $HC(NH_2)_2PbI_3$ *Adv. Mater.* **26** 4991–8

[62] Anon Fundamentals of Solar Cell Design | Wiley *Wiley.com*

[63] Anon A.Ibrahim, M.R.I.Ramadan, S.Aboul-Enein, A.A.ElSebaii, S.M.El-Broullesy,,"Short Circuit Current Isc as a Real Non-Destructive Diagnostic Tool of a Photovoltaic Modules Performance ",International Journal Of Renewable Energy Research, IJRER

[64] Pode R 2012 On the problem of open circuit voltage in metal phthalocyanine/C60 organic solar cells *Adv. Mater. Lett.* **2** 3–11

[65] O'Regan B and Gratzel M 1991 A low-cost, high-efficiency solar cell based on dyesensitized colloidal TiO2 films *Nature* **353** 737–40

[66] Grätzel M 2005 Solar Energy Conversion by Dye-Sensitized Photovoltaic Cells *Inorg. Chem.* **44** 6841–51

[67] Lee M M, Teuscher J, Miyasaka T, Murakami T N and Snaith H J 2012 Efficient Hybrid Solar Cells Based on Meso-Superstructured Organometal Halide Perovskites *Science* **338** 643–7

[68] Leijtens T, Stranks S D, Eperon G E, Lindblad R, Johansson E M J, McPherson I J, Rensmo H, Ball J M, Lee M M and Snaith H J 2014 Electronic Properties of Meso-Superstructured and Planar Organometal Halide Perovskite Films: Charge Trapping, Photodoping, and Carrier Mobility *ACS Nano* **8** 7147–55

[69] Xing G, Mathews N, Sun S, Lim S S, Lam Y M, Grätzel M, Mhaisalkar S and Sum T C 2013 Long-Range Balanced Electron- and Hole-Transport Lengths in Organic-Inorganic $CH_3NH_3PbI_3$ *Science* **342** 344–7

[70] Kim H-S, Im S H and Park N-G 2014 Organolead Halide Perovskite: New Horizons in Solar Cell Research *J. Phys. Chem. C* **118** 5615–25

[71] Heo J H, Im S H, Noh J H, Mandal T N, Lim C-S, Chang J A, Lee Y H, Kim H, Sarkar A, Nazeeruddin Md K, Grätzel M and Seok S I 2013 Efficient inorganic–organic hybrid heterojunction solar cells containing perovskite compound and polymeric hole conductors *Nat. Photonics* **7** 486–91

[72] Burschka J, Pellet N, Moon S-J, Humphry-Baker R, Gao P, Nazeeruddin M K and Grätzel M 2013 Sequential deposition as a route to high-performance perovskite-sensitized solar cells *Nature* **499** 316–9

[73] Im J-H, Jang I-H, Pellet N, Grätzel M and Park N-G 2014 Growth of CH3NH3PbI3 cuboids with controlled size for high-efficiency perovskite solar cells *Nat. Nanotechnol.* **9** 927–32

[74] Giordano F, Abate A, Correa Baena J P, Saliba M, Matsui T, Im S H, Zakeeruddin S M, Nazeeruddin M K, Hagfeldt A and Graetzel M 2016 Enhanced electronic properties in mesoporous TiO2 via lithium doping for high-efficiency perovskite solar cells *Nat. Commun.* **7** 10379

[75] Salim T, Sun S, Abe Y, Krishna A, Grimsdale A C and Lam Y M 2015 Perovskite-based solar cells: impact of morphology and device architecture on device performance *J. Mater. Chem. A* **3** 8943–69

[76] Eperon G E, Burlakov V M, Docampo P, Goriely A and Snaith H J 2014 Morphological Control for High Performance, Solution-Processed Planar Heterojunction Perovskite Solar Cells *Adv. Funct. Mater.* **24** 151–7

[77] Ball J M, Lee M M, Hey A and Snaith H J 2013 Low-temperature processed meso-superstructured to thin-film perovskite solar cells *Energy Environ. Sci.* **6** 1739

[78] Jiang Q, Zhang L, Wang H, Yang X, Meng J, Liu H, Yin Z, Wu J, Zhang X and You J 2017 Enhanced electron extraction using SnO2 for high-efficiency planar-structure HC(NH2)2PbI3-based perovskite solar cells *Nat. Energy* **2** 16177

[79] Seo J-Y, Matsui T, Luo J, Correa-Baena J-P, Giordano F, Saliba M, Schenk K, Ummadisingu A, Domanski K, Hadadian M, Hagfeldt A, Zakeeruddin S M, Steiner U, Grätzel M and Abate A 2016 Ionic Liquid Control Crystal Growth to Enhance Planar Perovskite Solar Cells Efficiency *Adv. Energy Mater.* **6** 1600767

[80] Anaraki E H, Kermanpur A, Steier L, Domanski K, Matsui T, Tress W, Saliba M, Abate A, Grätzel M, Hagfeldt A and Correa-Baena J-P 2016 Highly efficient and stable planar perovskite solar cells by solution-processed tin oxide *Energy Environ. Sci.* **9** 3128–34

[81] Leijtens T, Eperon G E, Noel N K, Habisreutinger S N, Petrozza A and Snaith H J 2015 Stability of Metal Halide Perovskite Solar Cells *Adv. Energy Mater.* **5** 1500963

[82] Jeng J-Y, Chiang Y-F, Lee M-H, Peng S-R, Guo T-F, Chen P and Wen T-C 2013 $CH_3NH_3PbI_3$ Perovskite/Fullerene Planar-Heterojunction Hybrid Solar Cells *Adv. Mater.* **25** 3727–32

[83] Sun S, Salim T, Mathews N, Duchamp M, Boothroyd C, Xing G, Sum T C and Lam Y M 2014 The origin of high efficiency in low-temperature solution-processable bilayer organometal halide hybrid solar cells *Energy Env. Sci* **7** 399–407

[84] Docampo P, Ball J M, Darwich M, Eperon G E and Snaith H J 2013 Efficient organometal trihalide perovskite planar-heterojunction solar cells on flexible polymer substrates *Nat. Commun.* **4** 2761

[85] You J, Hong Z, Yang Y (Michael), Chen Q, Cai M, Song T-B, Chen C-C, Lu S, Liu Y, Zhou H and Yang Y 2014 Low-Temperature Solution-Processed Perovskite Solar Cells with High Efficiency and Flexibility *ACS Nano* **8** 1674–80

[86] Malinkiewicz O, Yella A, Lee Y H, Espallargas G M, Graetzel M, Nazeeruddin M K and Bolink H J 2014 Perovskite solar cells employing organic charge-transport layers *Nat. Photonics* **8** 128–32

[87] Wang J T-W, Ball J M, Barea E M, Abate A, Alexander-Webber J A, Huang J, Saliba M, Mora-Sero I, Bisquert J, Snaith H J and Nicholas R J 2014 Low-Temperature Processed Electron Collection Layers of Graphene/TiO_2 Nanocomposites in Thin Film Perovskite Solar Cells *Nano Lett.* **14** 724–30

[88] Bai Y, Dong Q, Shao Y, Deng Y, Wang Q, Shen L, Wang D, Wei W and Huang J 2016 Enhancing stability and efficiency of perovskite solar cells with crosslinkable silane-functionalized and doped fullerene *Nat. Commun.* **7** 12806

[89] Liu D and Kelly T L 2014 Perovskite solar cells with a planar heterojunction structure prepared using room-temperature solution processing techniques *Nat. Photonics* **8** 133–8

[90] Ke W, Fang G, Liu Q, Xiong L, Qin P, Tao H, Wang J, Lei H, Li B, Wan J, Yang G and Yan Y 2015 Low-Temperature Solution-Processed Tin Oxide as an Alternative Electron Transporting Layer for Efficient Perovskite Solar Cells *J. Am. Chem. Soc.* **137** 6730–3

[91] Correa Baena J P, Steier L, Tress W, Saliba M, Neutzner S, Matsui T, Giordano F, Jacobsson T J, Srimath Kandada A R, Zakeeruddin S M, Petrozza A, Abate A, Nazeeruddin M K, Grätzel M and Hagfeldt A 2015 Highly efficient planar perovskite solar cells through band alignment engineering *Energy Environ. Sci.* **8** 2928–34

[92] Wang L, Fu W, Gu Z, Fan C, Yang X, Li H and Chen H 2014 Low temperature solution processed planar heterojunction perovskite solar cells with a CdSe nanocrystal as an electron transport/extraction layer *J Mater Chem C* **2** 9087–90

[93] Liu J, Gao C, Luo L, Ye Q, He X, Ouyang L, Guo X, Zhuang D, Liao C, Mei J and Lau W 2015 Low-temperature, solution processed metal sulfide as an electron transport layer for efficient planar perovskite solar cells *J. Mater. Chem. A* **3** 11750–5

[94] Chiang C-H, Tseng Z-L and Wu C-G 2014 Planar heterojunction perovskite/PC $_{71}$ BM solar cells with enhanced open-circuit voltage via a (2/1)-step spin-coating process *J Mater Chem A* **2** 15897–903

[95] Juarez-Perez E J, Wuβler M, Fabregat-Santiago F, Lakus-Wollny K, Mankel E, Mayer T, Jaegermann W and Mora-Sero I 2014 Role of the Selective Contacts in the Performance of Lead Halide Perovskite Solar Cells *J. Phys. Chem. Lett.* **5** 680–5

[96] Li X, Bi D, Yi C, Décoppet J-D, Luo J, Zakeeruddin S M, Hagfeldt A and Grätzel M 2016 A vacuum flash–assisted solution process for high-efficiency large-area perovskite solar cells *Science* **353** 58–62

[97] Song Z, Abate A, Watthage S C, Liyanage G K, Phillips A B, Steiner U, Graetzel M and Heben M J 2016 In-situ observation of moisture-induced degradation of perovskite solar cells using laser-beam induced current *2016 IEEE 43rd Photovoltaic Specialists Conference (PVSC)* 2016 IEEE 43rd Photovoltaic Specialists Conference (PVSC) (Portland, OR, USA: IEEE) pp 1202–6

[98] Song Z, Watthage S C, Phillips A B, Liyanage G K, Khanal R R, Tompkins B L, Ellingson R J and Heben M J 2015 Investigation of degradation mechanisms of perovskite-based photovoltaic devices using laser beam induced current mapping SPIE Optics + Photonics for Sustainable Energy ed L A Eldada and M J Heben (San Diego, California, United States) p 956107

[99] Song Z, Abate A, Watthage S C, Liyanage G K, Phillips A B, Steiner U, Graetzel M and Heben M J 2016 Perovskite Solar Cell Stability in Humid Air: Partially Reversible Phase Transitions in the PbI_2-CH_3NH_3I-H_2O System *Adv. Energy Mater.* **6** 1600846

[100] Guo Y, Liu C, Inoue K, Harano K, Tanaka H and Nakamura E 2014 Enhancement in the efficiency of an organic–inorganic hybrid solar cell with a doped P3HT hole-transporting layer on a void-free perovskite active layer *J Mater Chem A* **2** 13827–30

[101] Yang W S, Noh J H, Jeon N J, Kim Y C, Ryu S, Seo J and Seok S I 2015 High-performance photovoltaic perovskite layers fabricated through intramolecular exchange *Science* **348** 1234–7

[102] Rakstys K, Abate A, Dar M I, Gao P, Jankauskas V, Jacopin G, Kamarauskas E, Kazim S, Ahmad S, Grätzel M and Nazeeruddin M K 2015 Triazatruxene-Based Hole Transporting Materials for Highly Efficient Perovskite Solar Cells *J. Am. Chem. Soc.* **137** 16172–8

[103] Zhang Y, Elawad M, Yu Z, Jiang X, Lai J and Sun L 2016 Enhanced performance of perovskite solar cells with P3HT hole-transporting materials via molecular p-type doping *RSC Adv.* **6** 108888–95

[104] Jeng J-Y, Chen K-C, Chiang T-Y, Lin P-Y, Tsai T-D, Chang Y-C, Guo T-F, Chen P, Wen T-C and Hsu Y-J 2014 Nickel Oxide Electrode Interlayer in $CH_3NH_3PbI_3$ Perovskite/PCBM Planar-Heterojunction Hybrid Solar Cells *Adv. Mater.* **26** 4107–13

[105] Kim J H, Liang P-W, Williams S T, Cho N, Chueh C-C, Glaz M S, Ginger D S and Jen A K-Y 2015 High-Performance and Environmentally Stable Planar Heterojunction Perovskite Solar Cells Based on a Solution-Processed Copper-Doped Nickel Oxide Hole-Transporting Layer *Adv. Mater.* **27** 695–701

[106] Park J H, Seo J, Park S, Shin S S, Kim Y C, Jeon N J, Shin H-W, Ahn T K, Noh J H, Yoon S C, Hwang C S and Seok S I 2015 Efficient $CH_3NH_3PbI_3$ Perovskite Solar Cells Employing Nanostructured p-Type NiO Electrode Formed by a Pulsed Laser Deposition *Adv. Mater.* **27** 4013–9

[107] Li N, Zhu Z, Chueh C-C, Liu H, Peng B, Petrone A, Li X, Wang L and Jen A K-Y 2017 Mixed Cation $FA_xPEA_{1-x}PbI_3$ with Enhanced Phase and Ambient Stability toward High-Performance Perovskite Solar Cells *Adv. Energy Mater.* **7** 1601307

[108] Zuo C and Ding L 2015 Solution-Processed Cu_2O and CuO as Hole Transport Materials for Efficient Perovskite Solar Cells *Small* **11** 5528–32

[109] Ye S, Sun W, Li Y, Yan W, Peng H, Bian Z, Liu Z and Huang C 2015 CuSCN-Based Inverted Planar Perovskite Solar Cell with an Average PCE of 15.6% *Nano Lett.* **15** 3723–8

[110] Correa-Baena J-P, Abate A, Saliba M, Tress W, Jesper Jacobsson T, Grätzel M and Hagfeldt A 2017 The rapid evolution of highly efficient perovskite solar cells *Energy Environ. Sci.* **10** 710–27

[111] Chen B, Zheng X, Bai Y, Padture N P and Huang J 2017 Progress in Tandem Solar Cells Based on Hybrid Organic–Inorganic Perovskites *Adv. Energy Mater.* **7** 1602400

[112] Eperon G E, Stranks S D, Menelaou C, Johnston M B, Herz L M and Snaith H J 2014 Formamidinium lead trihalide: a broadly tunable perovskite for efficient planar heterojunction solar cells *Energy Environ. Sci.* **7** 982

[113] Kulkarni S A, Baikie T, Boix P P, Yantara N, Mathews N and Mhaisalkar S 2014 Band-gap tuning of lead halide perovskites using a sequential deposition process *J Mater Chem A* **2** 9221–5

[114] Noh J H, Im S H, Heo J H, Mandal T N and Seok S I 2013 Chemical Management for Colorful, Efficient, and Stable Inorganic–Organic Hybrid Nanostructured Solar Cells *Nano Lett.* **13** 1764–9

[115] Mosconi E, Amat A, Nazeeruddin Md K, Grätzel M and De Angelis F 2013 First-Principles Modeling of Mixed Halide Organometal Perovskites for Photovoltaic Applications *J. Phys. Chem. C* **117** 13902–13

[116] Colella S, Mosconi E, Fedeli P, Listorti A, Rizzo A, Gazza F and Orlandi F 2014 MAPbI3-xClx mixed halide perovskite for hybrid solar cells: the role of chloride as dopant on the transport and structural properties *Chem Mater* **25** 1–1

[117] Chen Q, Zhou H, Fang Y, Stieg A Z, Song T-B, Wang H-H, Xu X, Liu Y, Lu S, You J, Sun P, McKay J, Goorsky M S and Yang Y 2015 The optoelectronic role of chlorine in CH3NH3PbI3(Cl)-based perovskite solar cells *Nat. Commun.* **6** 7269

[118] Bi D, Tress W, Dar M I, Gao P, Luo J, Renevier C, Schenk K, Abate A, Giordano F, Correa Baena J-P, Decoppet J-D, Zakeeruddin S M, Nazeeruddin M K, Grätzel M and Hagfeldt A 2016 Efficient luminescent solar cells based on tailored mixed-cation perovskites *Sci. Adv.* **2** e1501170

[119] Gong J, Darling S B and You F 2015 Perovskite photovoltaics: life-cycle assessment of energy and environmental impacts *Energy Environ. Sci.* **8** 1953–68

[120] Celik I, Song Z, Cimaroli A J, Yan Y, Heben M J and Apul D 2016 Life Cycle Assessment (LCA) of perovskite PV cells projected from lab to fab *Sol. Energy Mater. Sol. Cells* **156** 157–69

[121] Noel N K, Stranks S D, Abate A, Wehrenfennig C, Guarnera S, Haghighirad A-A, Sadhanala A, Eperon G E, Pathak S K, Johnston M B, Petrozza A, Herz L M and Snaith H J 2014 Lead-free organic–inorganic tin halide perovskites for photovoltaic applications *Energy Env. Sci* **7** 3061–8

[122] Hao F, Stoumpos C C, Cao D H, Chang R P H and Kanatzidis M G 2014 Lead-free solid-state organic–inorganic halide perovskite solar cells *Nat. Photonics* **8** 489–94

[123] Ke W, Stoumpos C C, Logsdon J L, Wasielewski M R, Yan Y, Fang G and Kanatzidis M G 2016 TiO_2 –ZnS Cascade Electron Transport Layer for Efficient Formamidinium Tin Iodide Perovskite Solar Cells *J. Am. Chem. Soc.* **138** 14998–5003

[124] Ogomi Y, Morita A, Tsukamoto S, Saitho T, Fujikawa N, Shen Q, Toyoda T, Yoshino K, Pandey S S, Ma T and Hayase S 2014 $CH_3NH_3Sn_xPb_{(1-x)}I_3$ Perovskite Solar Cells Covering up to 1060 nm *J. Phys. Chem. Lett.* **5** 1004–11

[125] Zhao D, Yu Y, Wang C, Liao W, Shrestha N, Grice C R, Cimaroli A J, Guan L, Ellingson R J, Zhu K, Zhao X, Xiong R-G and Yan Y 2017 Low-bandgap mixed tin–lead iodide perovskite absorbers with long carrier lifetimes for all-perovskite tandem solar cells *Nat. Energy* **2** 17018

[126] Naceur I and Zeraoulia M 2019 *Qualitative study of Indium Gallium Nitride (InGaN) – based solar cell* (University of Biskra.)

[127] Drive P H and Clara S DEVICE SIMULATION SOFTWARE 1776

[128] Azri F 2022 *Study of hybrid organic-inorganic solar cells based on perovskite materials* (University of Biskra)

[129] Li C, Song Z, Zhao D, Xiao C, Subedi B, Shrestha N, Junda M M, Wang C, Jiang C, Al-Jassim M, Ellingson R J, Podraza N J, Zhu K and Yan Y 2019 Reducing Saturation-Current Density to Realize High-Efficiency Low-Bandgap Mixed Tin–Lead Halide Perovskite Solar Cells *Adv. Energy Mater.* **9** 1803135

[130] Matebese F, Taziwa R and Mutukwa D 2018 Progress on the Synthesis and Application of CuSCN Inorganic Hole Transport Material in Perovskite Solar Cells *Materials* **11** 2592

[131] Moyez S A, Maitra S, Mukherjee K, Sengupta A and Roy S 2020 Structural Features and Optical Properties of CH3NH3Pb(1−x)SnxCl3 Thin-Film Perovskites for Photovoltaic Applications *J. Electron. Mater.* **49** 7133–43

[132] Odysseas Kosmatos K, Theofylaktos L, Giannakaki E, Deligiannis D, Konstantakou M and Stergiopoulos T 2019 Methylammonium Chloride: A Key Additive for Highly Efficient, Stable, and Up-Scalable Perovskite Solar Cells *ENERGY Environ. Mater.* **2** 79–92

Abstract

The development and commercialization of perovskite solar cells (PSCs) is delayed by the toxicity of lead present in the perovskite, which is the solar light absorber material. To counter this problem, lead (Pb) can be partially replaced by diverse elements and among them we have chosen to study the tin (Sn). The study is based on numerical simulation by Silvaco-Atlas, which is a powerful software for 2D, and 3D electronic device's modelling. The simulated results are also compared with available measurement to certify the study. The studied PSC at the fist is FTO/TiO_2/MAPbI/ spiro-OMeTAD (n-i-p) that gave electrical outputs similar to experimental range; $J_{sc} = 27.91\frac{mA}{cm^2}, V_{oc} = 0.88\,V, FF = 0.72\,, PCE = 17.71\%$. After that and since the organic HTM (spiro-OMeTAD), according to many works, suffered from instability, we have replaced it by the inorganic HTM CuSCN and as results a slight further improvement was occurred in $J_{sc} = 28.15\frac{mA}{cm^2}$. Next we have concentrated on the main goal of the work with is replacing partially Pb by Sn by considering the $MAPbCl_3$ perovskite which has band gap of 2.92 eV. With 80% of Sn and 20% of Pb the band gap is reduced to 2.19 eV and the solar cell gave good electrical outputs similar to experimental data; $J_{sc} = 18.82\frac{mA}{cm^2}, V_{oc} = 1.26\,V, FF = 0.749\,, PCE = 17.76\%$.

The band gap reduction that occurs with the partial replacement of Pb with Sn is used in the design of a Tandem solar cell where the perovskite material of the top cell is $MAPb_{0.2}Sn_{0.8}Cl_3$ (2.19 eV) while that of the bottom one is $MAPb_{0.5}Sn_{0.5}I_3$ (1.18 eV). By considering the ideal performance of the cell a very interesting outputs was obtained: $J_{sc} = 18.82\frac{mA}{cm^2}, V_{oc} = 1.75\,V, FF = 0.804\,, PCE = 26.48\%$.

Key words : perovskite, solar cells, Pb_{1-x}-Sn_x, Silvaco-Atlas.

ملخص

تأخر تطوير و تسويق الخلايا الشمسية البيروفسكية بسبب سمية الرصاص الموجود في البيروفسكايت, و هي المادة التي تمتص ضوء الشمس. لمواجهة هذه المشكلة يمكن استبدال الرصاص (Pb) جزئيا بعناصر متنوعة و من بينها اخترنا دراسة القصدير (Sn). تعتمد هذه الدراسة على المحاكاة العددية بواسطة سلفاكو-أطلس, و هو برنامج ضخم لنمذجة الأجهزة الإلكترونية ثنائية و ثلاثية الأبعاد. كذلك تتم مقارنة نتائج المحاكاة بالنتائج التجريبية المقاسة للمصادقة على الدراسة. الخلية الشمسية البيروفكسية الأولى المدروسة مكونة من FTO/TiO_2/MAPbI/ spiro-OMeTAD (n-i-p) و التي اعطت وسائط الخروج الكهربائية

$$J_{sc} = 27.91\frac{mA}{cm^2}, V_{oc} = 0.88\,V, FF = 0.72\,, PCE = 17.71\%$$

.بعد ذلك، منذ إنشاء المادة العضوية الناقلة للثقوب HTM (spiro-OMeTAD) و وفقا للعديد من الأعمال عانت هذه المادة من عدم الإستقرار لذا أستبدلنا هذه المادة بمادة غير عضوية و هي CuScN و نتيجة لذلك حدث تحسن طفيف $J_{sc} = 28.15\frac{mA}{cm^2}$. بعد ذلك ركزنا على الهدف الرئيس للعمل و هي إستبدال Pb جزئيا بواسطة Sn من خلال البيروفسكايت $MAPbCl_3$ و الذي لديه نطاق طاقة 2.92 eV. مع 80% من القصدير و 20% من الرصاص يتم تقليل نطاق الطاقة الى 2.19eV و أعطت الخلية الشمسية وسائط خروج كهربائية مماثلة للتجريبية

$$J_{sc} = 18.82\frac{mA}{cm^2}, V_{oc} = 1.26\,V, FF = 0.749\,, PCE = 17.76\%:$$

يتم استخدام تقليل نطاق الطاقة الذي يحدث مع الإستبدال الجزئي للرصاص Pb بالقصدير Sn في تصميم خلية شمسية ترادفية بحيث تكون مادة البيروفسكايت للخلية العلوية هي $MAPb_{0.2}Sn_{0.8}Cl_3$ (2.19 eV). بينما تكون السفلية هي $MAPb_{0.5}Sn_{0.5}I_3$ (1.18 eV) . من خلال النظر في الأداء المثالي للخلية تم الحصول وسائط الخروج مثيرة للاهتمام :

$$J_{sc} = 18.82\frac{mA}{cm^2}, V_{oc} = 1.75\,V, FF = 0.804\,, PCE = 26.48\%.$$

الكلمات المفتاحية : بيروفسكايت، خلية شمسية، Pb_{1-x}-Sn_x ، سلفاكو-أطلس.